Scala vestibuli pressure and three-dimensional stapes velocity measured in direct succession in gerbil[a)]

W. F. Decraemer[b)]
University of Antwerp, CGB, Groenenborgerlaan 171, B-2020 Antwerpen, Belgium

O. de La Rochefoucauld, W. Dong, and S. M. Khanna
Columbia University, 630 West 168th Street, New York, New York 10032

J. J. J. Dirckx
University of Antwerp, CGB, Groenenborgerlaan 171, B-2020 Antwerpen, Belgium

E. S. Olson
Columbia University, 630 West 168th Street, New York, New York 10032

(Received 23 October 2006; revised 25 January 2007; accepted 25 January 2007)

It was shown that the mode of vibration of the stapes has a predominant piston component but rotations producing tilt of the footplate are also present. Tilt and piston components vary with frequency. Separately it was shown that the pressure gain between ear canal and scala vestibuli was a remarkably flat and smooth function of frequency. Is tilt functional contributing to the pressure in the scala vestibuli and helping in smoothing the pressure gain? In experiments on gerbil the pressure in the scala vestibuli directly behind the footplate was measured while recording simultaneously the pressure produced by the sound source in the ear canal. Successively the three-dimensional motion of the stapes was measured in the same animal. Combining the vibration measurements with an anatomical shape measurement from a micro-CT (CT: computed tomography) scan the piston-like motion and the tilt of the footplate was calculated and correlated to the corresponding scala vestibuli pressure curves. No evidence was found for the hypothesis that dips in the piston velocity are filled by peaks in tilt in a systematic way to produce a smooth middle ear pressure gain function. The present data allowed calculations of the individual cochlear input impedances. © *2007 Acoustical Society of America.* [DOI: 10.1121/1.2709843]

PACS number(s): 43.64.Ha, 43.64.Kc, 43.64.Yp [BLM] Pages: 2774–2791

I. INTRODUCTION

The motion of the stapes footplate defines the mechanical middle ear output and produces the acoustical input to the cochlea. The mode of stapes vibration (piston-like and/or rocking) has been studied mainly in human temporal bones [for an overview see Heiland *et al.* (1999) and Hato *et al.* (2003)] and in a few animal models [anesthetized cat, Guinan and Peake (1967); cat temporal bone, Decraemer *et al.* (2003) and Decraemer and Khanna (2003); gerbil, Olson and Cooper (2000)]. Older measurements made use of capacitive probes, stroboscopic microscopy, and time-averaged holography, while the more recent measurements all made use of heterodyne laser interferometers, improving measurement quality and expanding the frequency range of measurements to most of the audible range. It is now well established that the motion is not purely piston-like but that at higher frequencies rotations about the long and short footplate axis are also present ("rocking," "tilting"). Whether the nonpiston motion components are functionally important is an open question. An argument in favor is the remarkable ability of the middle-ear to produce a gain between the sound pressure in the ear canal and the acoustic pressure in the perilymph of the scala vestibuli (directly behind the footplate) that is a very smooth function of frequency (Olson, 1998; Puria *et al.*, 1997) while the frequency response of the stapes exhibits pronounced maxima and minima. Could it be that tilting of the footplate of the stapes fills in the gaps in the frequency response of the piston component resulting in a smoother pressure frequency response in the cochlea? (Let us at this point make clear that when we call a function "smooth" in this paper we mean "with small differences between contiguous data points"). In an attempt to answer this question we have measured the scala vestibuli (SV) pressure using a micropressure sensor (Olson, 1998, 2001) followed by a measurement of the three-dimensional (3D) vibration velocity of the stapes in the adult gerbil using a confocal heterodyne microscope/interferometer (Decraemer and Khanna, 1999). We show the results for three animals. The pressure results are presented quite directly. The motion results require analysis to present them in the most useful coordinate system, and the issue of propagation of experimen-

[a)]Portions of this work were presented in "Is the scala vestibuli pressure influenced by non-piston like stapes motion components? An experimental approach," Proceedings of Auditory Mechanisms and Models, Portland, OR, July 2005, and "Do non-piston components contribute to scala vestibuli pressure behind the footplate in gerbil?," Proceedings of the International Symposium on Middle Ear Mechanics in Research and Otology, Zurich, Switzerland, July 2006.

[b)]Electronic mail: wim.decraemer@ua.ac.be

tal error is presented in some detail. Finally we combine the pressure and velocity measurements, to find the cochlear input impedance.

II. MATERIAL AND METHODS

A. Animal preparation

Measurements were performed in three gerbils, 50–70 g in mass. The animal was first sedated with ketamine (1 mg/kg) and then deeply anaesthetized with sodium pentobarbital (initial dose 60 mg/kg). Supplemental doses (10 mg/kg) were given when a toe pinch response was elicited (checked at least every 20 min). The body temperature was maintained at 37 °C using an animal blanket. The animal head was firmly attached to a head holder using dental cement and surgery was performed to expose the left cochlea. A tracheotomy was performed to maintain a clear airway. Due to the length of the two-stage experiment (first SV pressure, then stapes motion) and the necessity of manipulating the animal when bringing it from one setup to the other, the animals did not survive during the entire second part of the experiment. The experiment was, without interruption, continued on the fresh cadaver. Animal 20m4 died during the last few runs of the 3D experiment (about 10 min before completion of the ~2.5 h experiment), animal 25m5 died after about 1 h and we restarted the entire 3D measurement. Animal 27m4 died after preparative surgery, all measurements were done on the fresh cadaver. The just post-mortem condition did not produce SV pressure or stapes velocity results that were significantly different.

The care and use of animals were approved by the Institutional Animal Care and Use Committee of Columbia University.

B. Sound system and pressure measurement in the ear canal

The external ear canal (EC) was cut short to its bony end and a small plastic tube with a diameter comparable to that of the EC was cemented in place. A sound delivery tube coupled to a sound source was tightly inserted in the plastic insert. A probe tube microphone was inserted coaxially within this tube and protruded slightly from the end within the EC. It measured the sound about 1 mm lateral from the superior edge of the pars tensa. Details of the sound source, sound delivery tube with coaxial probe microphone and microphone calibration have been described in detail previously (Khanna and Stinson, 1985).

The same sound driver and probe microphone were first used during the SV pressure measurements and later for the stapes velocity measurements. They had to be removed and replaced between the two stages of the experiment. Input to the sound driver was kept constant which resulted in a sound level in the EC that fluctuated slightly around 90 dB SPL.

C. Pressure measurements in the scala vestibuli

The intracochlear pressure in the SV was measured using a fiber-optic based micropressure sensor (diameter 170 μm) whose construction and calibration were described in Olson (1998). The sensitivity of the sensors is flat to within a few decibels up to at least 40 kHz. The sensors are calibrated the day of the experiment but the sensitivity is somewhat uncertain, as changes in sensor sensitivity from day to day or after an experiment of ~10 dB are not uncommon. These changes are flat with frequency, but set a limit on the accuracy of the absolute pressure. The sensitivity changes are likely a result of the fragility of the sensor membrane. To measure the pressure in the SV a small hole, the size of the pressure sensor, was hand drilled in the cochlear wall (Olson, 1998, Fig. 3). The pressure sensor was inserted to a depth of 100–200 μm with the aid of a micromanipulator. The distance with respect to the footplate was about 0.3 mm. This estimate was made later on a 3D model of the cochlea with inserted sensor, based on a micro CT scan of one of the temporal bones harvested at the end of the experiment (Dong and Olson, 2006, Fig. 1).

D. Hearing threshold measurements

An electrode was positioned at the round window opening to measure the compound action potential (CAP) response of the auditory nerve to tone pips as a measure of cochlear condition (Johnstone *et al.*, 1979). The CAP response was measured prior to other measurements in the live animals 20m4 and 25m4. Both showed a starting CAP threshold curve that was typical for normal hearing animals with thresholds of 20–30 dB SPL over the most sensitive hearing range (0.5–22 kHz). Above 22 kHz the thresholds of the two animals diverged, and variability is typical of this vulnerable region of the cochlea. In animal 20m4, the 35 kHz threshold was 60 dB, in 25m4 the 40 kHz threshold was 40 dB.

E. Simultaneous stapes velocity and ear canal pressure measurements

After completion of the SV pressure measurement the sensor was removed. The tiny hole in the cochlea was left open. The hole in the middle ear cavity used for hearing threshold measurement was made wide enough (about 5–6 mm in a direction parallel to the annulus) to allow a good view of the stapes. As we see in Fig. 1 the stapes head and the 2/3rd upper part of the crura are visible. Note that with this approach we observed the stapes in the living gerbil from almost the opposite direction to that used for previous stapes measurements in cat temporal bone (Decraemer and Khanna, 2000; Decraemer *et al.*, 2000). The approach allowed for a variation in observation angle of about ±15°, which is sufficient to determine the 3D components of the stapes motion. To prevent drying out of the specimen while the cavity was widely opened, small pieces (about 2 by 3 mm^2) of paper towel soaked in water were placed against the inner middle ear cavity wall in the space under the malleus handle. We took great care not to touch vibrating structures. In a later experiment during the motion measurement the specimen was also kept in the mist of an ultrasonic humidifier conducted via a plastic hose (diameter 1 cm) to

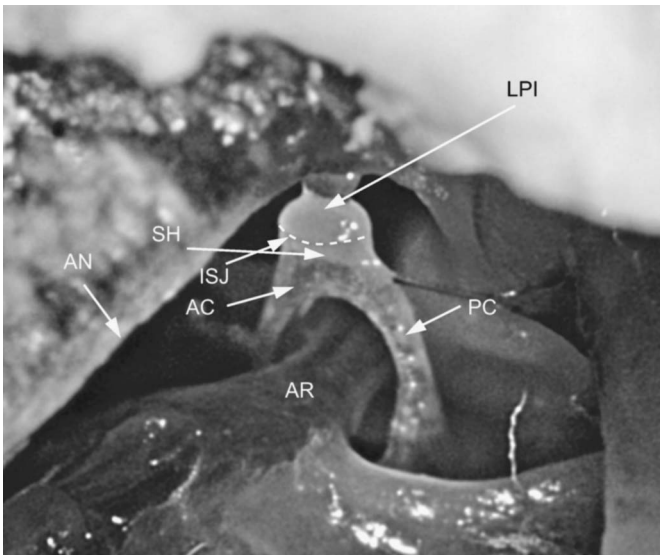

FIG. 1. A view of the stapes through a hole in the posterior ventral part of the bulla wall: LPI: lenticular process of the incus; SH: stapes head; ISJ: position of the incudo-stapedial joint; AC: anterior crus; PC: posterior crus; AN: part of the tympanic annulus; AR: artery running between the crura and blocking the view of the footplate.

about 2 cm from the opening in the bulla wall. These extra precautions did not markedly increase the already good stability of the preparation.

The velocity measurements were performed with a noncommercial heterodyne laser interferometer which is combined with a visual microscope (Khanna *et al.*, 1996). The focused laser beam coincides with the center of the image of the microscope displayed on a video monitor; the microscope allows visualization of the stapes, while the interferometer measures the vibration at the selected location in response to sound applied to the ear.

For the velocity measurements the animal's body was resting on an object support, while its head was immobilized by firmly clamping the head holder, which was cemented to the exposed top surface of the skull, to a post affixed to the positioning system. The positioning device provides micrometer positioning (with read-out of the coordinates) in three orthogonal directions (x,y,z) and allows changing the observation direction by means of two large, nested goniometers that are precisely aligned to rotate the object about the point of focus of the laser beam. (For details on this alignment see Appendix A.) The accuracy on the x,y,z coordinates is on the order of $5-10$ μm. It was determined by repeatedly focusing the interferometer beam on a given point while moving far away from this point intermediately. This small error is a combined result of the high sectioning depth of the interferometer (the interferometer carrier is 3 dB down at a distance of ± 13 μm) and the good positioning reproducibility of the translational stages.

The sound source and sound driver were put back in the EC insert in a position closely equal to that during SV pressure measurement. With the goniometers in their midposition $(H=0°, V=0°)$ the stapes was imaged, and we focused precisely on a chosen reference point (e.g., on the stapes head) and the coordinate read-out system was reset. For a set of points (typically seven to eight) as widely spread as possible on the entire visible part of the stapes we recorded the velocity of the stapes in response to pure tone stimuli, generated with a constant voltage input to the driver (SPL ranging from 85 to 95 dB up to 30 kHz and dropping to a lowest values of 70 dB at 40 kHz). The frequency was stepped between 200 Hz and 1 kHz with a step of 200 Hz, between 1 and 10 kHz with 250 Hz, between 10 and 20 kHz with 500 Hz, and between 20 and 50 kHz with 1000 Hz. For further processing all velocities (amplitude and phase) were expressed relative to the simultaneously measured EC pressure.

Using only one goniometer at a time, the stapes was rotated maximally in positive and negative directions without losing its image in the microscope (which occurs when the bulla wall blocks the illumination and interferometer laser beam). At each extreme angular position new velocity measurements were recorded. The procedure was sped up by storing the coordinates of the observation points used at $H=0°$, $V=0°$ and refocusing on the points automatically, using stepper motors driving the x,y,z positioning system. Note that (i) the coordinate readings for a given observation point in focus did not change when the object was rotated, as the rotation center coincided with the focused point and (ii) that for calculation of 3D rigid body motion components it is not mandatory to measure at the same points for different observation angles; if an observation point was no longer accessible after rotation of the object it was replaced by another point. This freedom of changing the observation points when using a different observation direction comes in very handy and is a result of a modification we made to the procedure we used hitherto to determine the 3D components of the malleus (Decraemer and Khanna, 1996) and stapes (Decraemer and Khanna, 2000; Decraemer *et al.*, 2000).

It is also important to point out that during the rotation the animal, sound driver, and probe microphone moved together as they were all mounted to the same object holder post of the positioning system keeping relative positions unchanged.

F. Processing of the data

1. 3D velocity components in the experimental reference system

In earlier studies on malleus and stapes vibration in cat (Decraemer and Khanna, 1996, 2000; Decraemer *et al.*, 2000) we determined the 3D motion in two steps. First the 3D velocity components of at least three points on a given ossicle were calculated and in a second step these results were used to calculate the 3D rigid body motion of the ossicle. To calculate the 3D components for a given point we had to observe the same point from several observation angles. This constraint is now relaxed: different points can be observed. The coordinates of all observation points and the amplitude and phase of the velocity at these points for all (here five) observation directions were used in a single fit to calculate the rigid-body motion components directly. These values describe the motion as the translation of a reference point on the body and the rotation of the body about this point. We determined the complete 3D motion, and thus

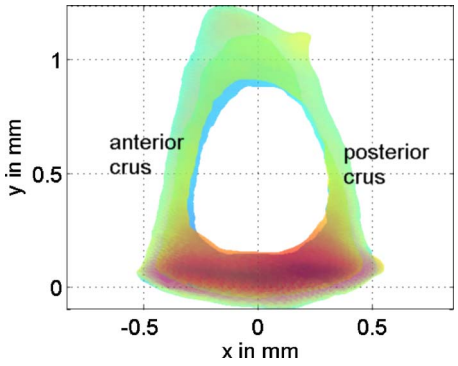

FIG. 2. (Color online) A 3D model of a gerbil stapes is brought in an intrinsic reference frame: The origin is at the footplate center, the x axis follows the long footplate axis in the posterior direction, the y axis is perpendicular to the footplate directed to the center of the stapes head, and the z axis is pointing out of the figure plane to the reader and follows the short axis in the inferior direction.

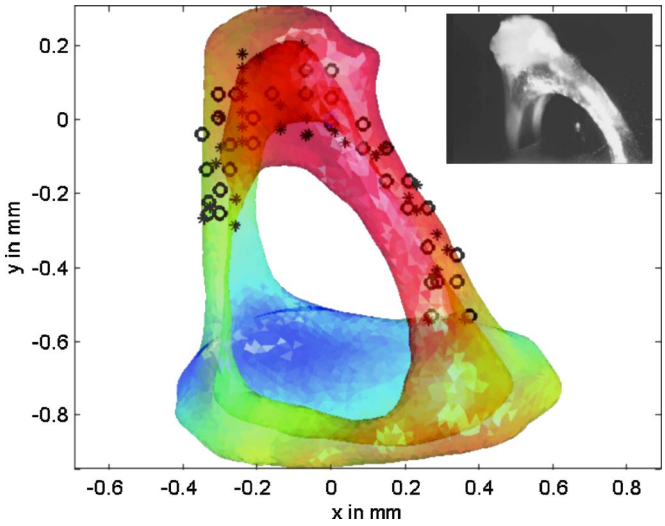

FIG. 3. (Color online) The model of the stapes is shown after registration in the position of the stapes during the experiment defined by the observation points (stars) and the extra set of "anatomical points" (circles). The insert at the top right shows a view of the stapes through the microscope during the experiment.

three components of both the translation and rotation vectors. Details of the mathematical procedure are given in Appendix B.

The assumption of rigid body behavior made during this calculation might seem questionable at first, the stapes of gerbil being such a thin and fragile structure. Its special design, however, with its two symmetrical widely spread crura with thin strongly curved walls and with its bowl-shaped footplate reinforced by an upstanding rim make it extremely light and sturdy at the same time (see the 3D stapes model in Fig. 2 or for a more detailed stapes model see Decraemer *et al.*, 2003).

Note that the motion components that we first obtain are expressed in the original coordinate system used during the experiment. In this reference system the object under study is quite arbitrarily oriented, which makes the straightforward interpretation of the frequency responses of the rotation and translation components almost impossible. In the next section we will explain how we can transform these components in a meaningful intrinsic coordinate system for the stapes.

2. 3D velocity components in an intrinsic reference system

As we are especially interested in the piston and the tilting components of the footplate we express the rigid-body motion components of the stapes in the following intrinsic reference frame: the origin at the center of the footplate, the x axis pointing in the posterior direction along the long axis of the footplate, the y axis perpendicular to the footplate pointing to the center of the stapes head, and the z axis running along the short axis of the footplate, completing a right-handed reference system (Fig. 2).

To calculate the motion components in the intrinsic reference system we first determined the coordinate transform that rotates the stapes from its experimental position into a position parallel to its position in the intrinsic frame and then shifted the stapes to let the origin coincide with the footplate center. We determine this transform in an intermediate step using a 3D stapes model as described in the following (Sec. II F 2 a). The coordinate transform that brings the stapes model from the experimental into the intrinsic frame will also transform the translation and rotation vectors in the intrinsic reference frame as explained in Appendix C.

a. Constructing and registering a 3D stapes model. Based on a micro-CT (CT: computed tomography) scan of the excised experimental ear we constructed a 3D model of the stapes. This model is defined in the reference system of the CT scanner which again is different from the experimental reference system as it depends on the position and orientation of the temporal bone during the scan. In a first step the model was registered in the reference frame that was used during the experiment and in which the coordinates of observation points and stapes vibration were recorded. The registration was done with an iterative closest point procedure described by Besl and McKay (1992). The number of observation points at which velocity was measured (less than 20) was too small to define the position of the stapes during the experiment with sufficient precision to make an accurate registration. To enhance registration, during the motion experiment we measured the coordinates of an extra set of about 50 "anatomical" points. This was a fast measurement that consisted of focusing the laser of the interferometer at points spread across the entire visible part of the stapes and automatically recording the coordinates (without vibration measurements). The procedures to make the 3D model and to register the model were described in a previous paper (Decraemer *et al.*, 2003). The 3D model registered in the set of experimental (stars) and anatomical points (circles), along with a picture of the stapes taken during the experiment through the microscope (insert) are shown in Fig. 3.

b. Coordinate transform from experimental to intrinsic frame. In a second step the model in the experimental reference frame was iteratively rotated about the x, y, and z axes until it was in a position parallel to its intrinsic position. In this way we obtained the rotation matrix of the required coordinate transformation. The vector from the experimental origin to the center of the footplate (new origin) determines the origin shift, completing the coordinate transform. The stapes in its intrinsic reference frame is shown in Fig. 2.

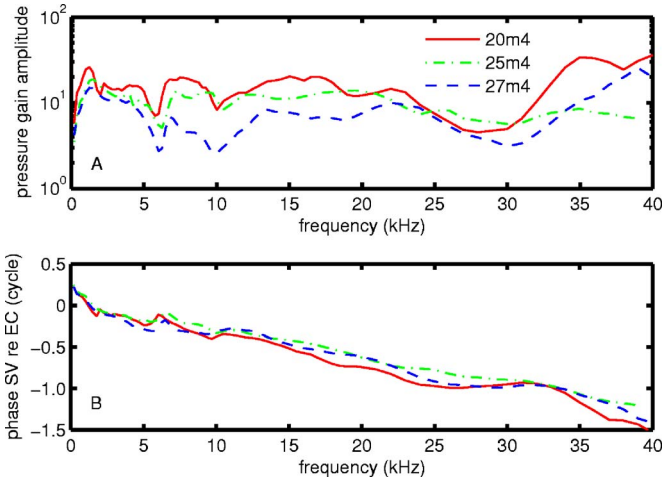

FIG. 4. (Color online) Pressure in the scala vestibuli relative to EC pressure ("middle ear pressure gain") is shown for three animals, 20m4, 25m4, and 27m4 (see legend). The amplitude of the gain (upper panel) is smooth with frequency, and varies in a small band around a level of ~10 (20 dB). The phases of the gain (lower panel) for all three animals were similar; the three curves start at +1/4 cycle at 190 Hz, rapidly decrease to 0 cycle at about 1.5 kHz where we observe a small peak, and decrease further to about 6 kHz where a second small peak is seen. From then the three phase curves show a gradual and approximately linear decrease with frequency to a total phase lag of about −1.5 cycle at 40 kHz.

G. Relative phase between pressure sensor and interferometer

In order to couple the measured pressures and velocities, we need to know the difference in the processing between the pressure sensor and the interferometer, in particular the relative phases of the two systems. The pressure sensor is composed of a gold-coated thin film membrane, whose position is interrogated by light emitting diode (LED) light via a fiber-optic lever. An optic lever is a simple displacement sensor, whose output is a voltage whose variations are proportional to displacement. To determine the relative phase between the interferometer and sensor we focused the interferometer laser on the sensor membrane. We drove the membrane with a free-field harmonic sound source while simultaneously monitoring its velocity with the interferometer on one side and its displacement with the sensor's optic lever on the other side. To compare amplitudes, we divided the reported velocity by ω. The displacement versus frequency measured with the interferometer and pressure sensor optics had very similar shapes in amplitude, and a relative phase that was a nearly straight line, indicative of a delay. The interferometer's demodulation electronics (a commercial REVOX FM demodulator) are based on a delay line that we knew produced a delay of ~15 μs (Willemin *et al.*, 1988). In our data, the phase-frequency data were well fit by a straight line with 14.1 μs delay, and this correction was used to compare interferometer and pressure sensor outputs.

III. RESULTS

A. Scala vestibuli pressure

Pressure in the SV relative to EC pressure is shown for three animals, 20m4, 25m4, and 27m4, in Fig. 4. These curves represent the pressure gain produced in the middle ear: the gain amplitude [Fig. 4(a)] was a smooth function of frequency, fluctuating in a small band around a level of 10 (20.0 dB) with extreme values of 3 (9.5 dB) and 20 (26.0 dB). In the low frequency tail the three animals showed a fast increase in gain with frequency resulting in a small maximum at ~1.5 kHz, followed by a steady decrease producing a minimum at about 6 kHz. The gain was again somewhat higher in a short frequency interval ending with a small dip at 10 kHz. For animal 25m4 (dashed dotted line) the gain was remarkably constant all the way up to the highest frequencies measured. Animals 20m4 and 27m4 had a broad and shallow minimum at 30 kHz, followed by a rise to their overall highest values.

Phase for all three animals was very similar [Fig. 4(b)]: the three curves started at +0.25 cycle at 190 Hz, rapidly decreased to 0 cycle at about 1.5 kHz (here the amplitude showed a small peak), then decreased further to about 6 kHz where a small peak appeared (here the amplitudes produced a dip). From then on the phases for all animals decreased linearly with frequency and a total phase lag of about −1.5 cycle had accumulated by 40 kHz. These results, particularly the flat magnitude and linear phase were shown in Olson (1998) and Dong and Olson (2006). Some systematic reasons for variations in results in different experiments, particularly in gain, were discussed in detail in Dong and Olson (2006).

B. Three-dimensional stapes velocity

1. Measurement accuracy based on repeatability: Comparison of changes due to observation angle with changes developing in time

In order to determine the 3D rigid body motion of the stapes we must perform repeated vibration measurements from different observation angles. Optimally we would like to measure along three orthogonal directions and spread the observation points over the entire ossicle. The anatomy of the middle ear does not provide such access for uniaxial interferometric measurements; only a limited part of the stapes is visible (Fig. 1) and variations in the observation angle are typically limited to ±15° to 20°. The changes in vibration for these relatively small angle variations are consequently also small. High measuring sensitivity is required and we must minimize changes with time by, e.g., letting the temperature stabilize, preventing desiccation, and by reducing total recording time. Figure 5 shows first the repeatability of the frequency responses for amplitude [Fig. 5(a)] and phase [Fig. 5(b)] of the displacement normalized to sound pressure level at a single point recorded with the goniometers set at $H=0°$ and $V=0°$. Figure 5 shows the mean and standard deviation for four runs (three repeats recorded within 7 min and one repeat measurement made 40 min later as a control measurement in the further course of the experiment), at a given reference point that was chosen at a retraceable detail in the image, e.g., at the middle of the stapes head. Figure 5 shows also the variation in response to changes in observation angle ($H=0°$, −15°, and +12°, and all $V=0°$) at a second observation point, halfway down on the posterior crus. We see that at most frequencies the change

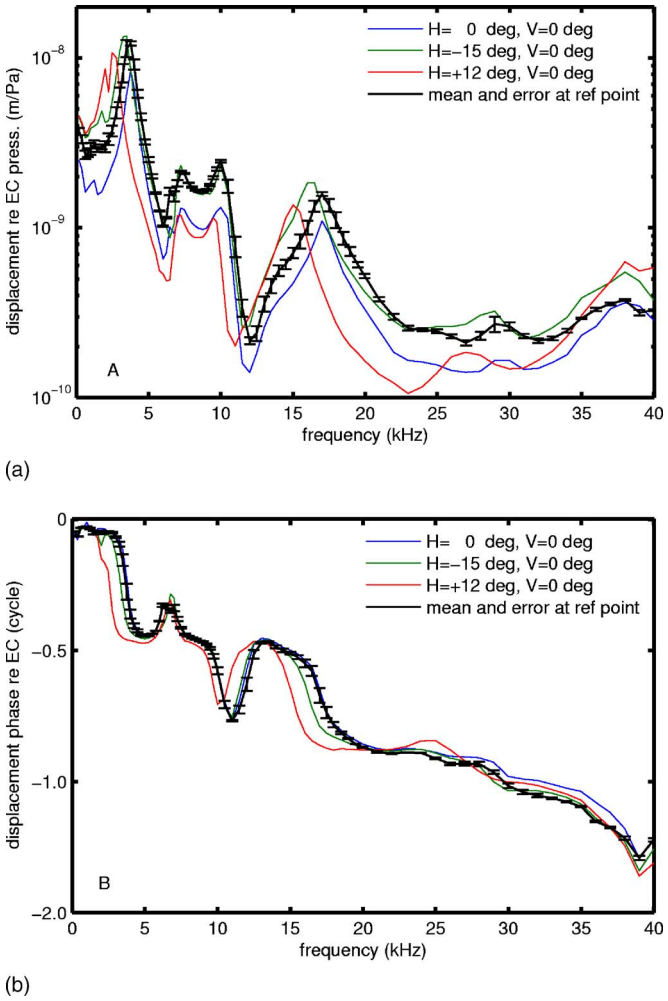

FIG. 5. (Color online) Repeatability of frequency responses for the amplitude (A) and the phase (B) of the displacement (per EC pressure) at a single point is shown by plotting the mean and its standard deviation for four runs (three repeats recorded in a time window of 7 min, and one control, 40 min after the last run, all with $H=0$ and $V=0$). At a different position, measurements were performed for three observation angles. The variation in response with observation angle at this point is also shown by plotting frequency responses for the different viewing angles (see the legend). The spread in change with observation angle for both amplitude and phase is at most frequencies substantially larger than the measurement uncertainty.

with observation angle of both amplitude and phase was substantially larger than the measurement uncertainty (here quantified by the repeatability of the measurements), as required. As we show results for two different observation points one can also judge the changes that are observed due to a change of the observation point by comparing the plot at $H=0°$, $V=0°$ with the curve showing the mean for the four runs at the same angle.

2. Rotation and translation frequency responses of the stapes in the experimental reference frame

Rigid body motion is described by three translation and three rotation components. In this and the next section we will show motion as rotational and translational displacement per unit pressure. These results were found using the methods of Appendix B operating on data like that in Fig. 5. Later, some of the displacement components will be converted into velocity and correlated with SV pressure in order

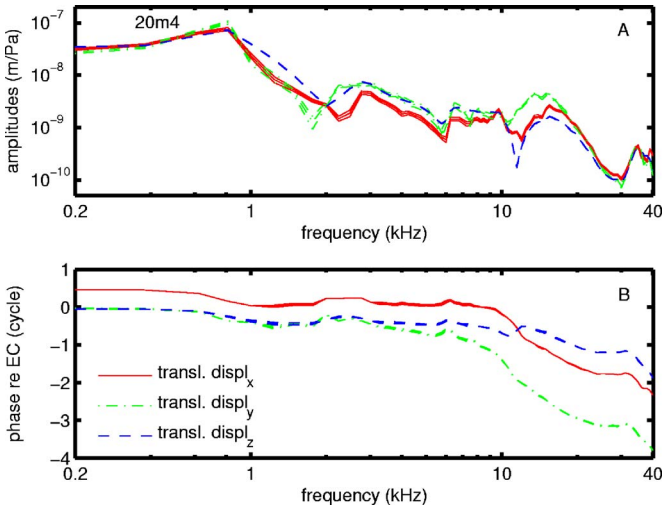

FIG. 6. (Color online) Frequency response for the three components of the translation displacement per EC sound pressure, expressed in the experimental reference frame. The experimental error, determined using a Monte Carlo method, is shown by plotting the curves with the component value + error and component value − error. The errors are small compared with the overall variations with frequency; translation displacement amplitudes (A) and phases (B) were determined with good accuracy.

to find acoustic impedance. We present results for the stapes of one gerbil (20m4). Figure 6 shows translation, Fig. 7 shows rotation. The components were calculated in the reference frame of the experiment. The different line types for the x, y, and z components are clarified in the legend. Due to the arbitrary nature of the experimental reference frame, the displacement components are difficult to interpret. Of major importance however is the question of how accurately these components can be determined. We therefore postpone the discussion of their significance until they are recalculated in the intrinsic frame and we restrict the discussion here to the error calculation.

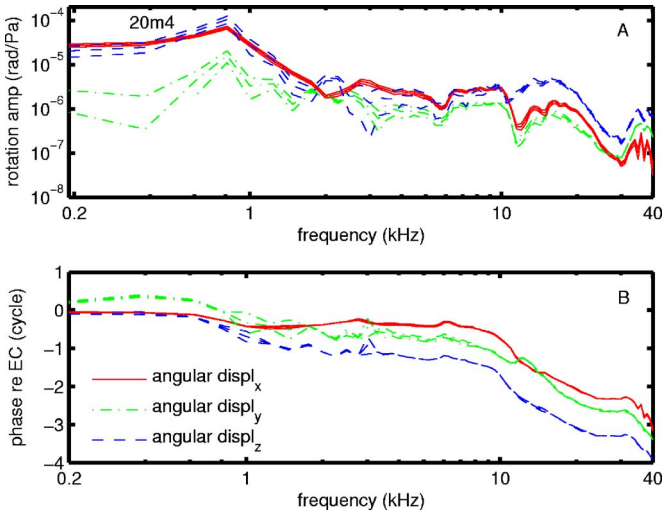

FIG. 7. (Color online) Frequency response for the three components of the rotation displacement per EC sound pressure, expressed in the experimental reference frame. The experimental error, determined using a Monte Carlo method, is shown by plotting curves with the component value + error and − error, as in Fig. 6. The errors on the rotational motion values are somewhat larger than those on the translation component values, but still show good accuracy.

The motion components were obtained with the method of Appendix B, using a least-squares fit with observations at all angles given the same weight. The estimate of the motion uncertainty (standard error) was obtained using a Monte Carlo method (Press *et al.*, 1989). To apply this technique we produced a large number (100) of new "experimental" data sets (frequency by frequency) by adding random noise drawn from a normal distribution (with a mean of zero and a variance chosen in agreement with the experimental uncertainty) to the observed amplitudes and phases and recalculated the fit for each set of data. The uncertainty in a displacement or rotation value was calculated as the standard deviation of all values obtained for this parameter. The variances used in this process to generate new data sets were the absolute error corresponding to a relative error of 0.05 in the amplitude and an absolute error of 0.1 rad in the phase of the measured vibration. The variance values were based on averages over all stimulus frequencies of the standard deviations in amplitude and phase for repeated observations at the same location, some measured in direct succession, some after intermediate measurements at other locations as explained in Sec. III B 1. The errors found using the Monte Carlo data to derive angular and translation displacements are indicated in Figs. 6 and 7 by plotting the nominal displacement values (without added noise) plus and minus their statistical error. The logarithmic scale for the amplitudes and the large span of the phase data tend to make the errors look small (some traces nearly or completely overlap), but nevertheless it is obvious that the obtained accuracy was good; the mostly smooth up and downward going trend in the curves is genuine and not due to noise in the observations as this would have generated jagged frequency responses. Errors on rotation components tend to be larger than errors on translation components. The errors that were obtained using the Monte Carlo method are in perfect accordance with errors that were obtained from a weighted fit procedure—an observation is given more weight when its experimental error is smaller—which simultaneously produced errors on the rigid body velocities as elements of the covariance matrix (Press *et al.*, 1989). The weights were also chosen on the basis of a constant relative error on the amplitude and constant absolute error on the phase and were then converted into weights on the in-phase and out-of-phase components (cf. Appendix B). We obtained frequency curves that showed the same overall trend as those from the unweighted fit, but the curves showed a few sudden spikes, most probably caused by strong fluctuations of the in- and out-of-phase components as they are calculated as the amplitude times the sine and cosine of the phase angle. For this reason, for its intuitive simplicity and in view of its ease in transforming the errors in another reference system (Sec. III B 3) the Monte Carlo error calculation method was finally retained.

The goodness-of-fit was also estimated by the calculation of the mean deviation between the experimental amplitude and phase and their fitted counterparts. For the amplitude we obtained a typical mean relative deviation between 10% and 20%, for the phase a mean absolute deviation typically between 5° and 15°. We think that these are very acceptable values, seen that for a given frequency the amplitudes of all observation points at all observation angles typically change within a factor of 3–10. Apart from the experimental uncertainty in the direct measurement, some of these deviations are caused by changes with time of the animal preparation that cannot be avoided when performing an extended experiment.

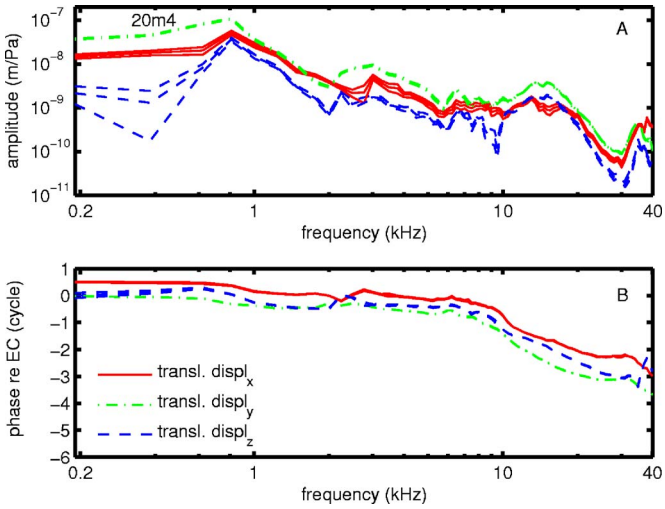

FIG. 8. (Color online) Frequency response for the translation displacement components per EC sound pressure for animal 20m4 expressed in the intrinsic reference system as defined in Fig. 2. (A) Amplitudes and (B) phases. Uncertainties are shown by plotting component + error and component − error curves. We see that peaks and valleys are genuine and that the piston component (dashed-dotted line) is most accurately determined (smaller error).

Let us mention at this time that the good quality of the rigid body model fit to the observed motion is indicating that the assumption of rigid body behavior is acceptable. This can be contrasted with the previous measurements of some of the authors (Decraemer *et al.*, 1994b) of manubrium motion. Unlike the compact stapes, the manubrium has an extended beam-like geometry. In that case, experiments clearly showed the existence of a bending mode on the thinnest part of the manubrium close to the umbo. In experiments to describe the 3D ossicular motion (Decraemer and Khanna, 1999, 2000), no observation points at this location were used. It is most probable that a structure such as a stapes will also have bending modes, but our results suggest that they add only to a small extent to the total velocity at a given point.

3. Rotation and translation frequency responses of the stapes in the intrinsic reference frame

To interpret the motion components they were transformed into the intrinsic frame of reference for the stapes as defined in Fig. 2. We have displayed components for three animals, 20m4 (translation: Fig. 8 and rotation: Fig. 9), 25m4 (translation: Fig. 10 and rotation: Fig. 11), and 27m4 (translation: Fig. 12 and rotation: Fig. 13), with amplitude (displacement normalized to EC pressure) in the upper panels (A) and phase (relative to EC phase) in the lower panels (B), to illustrate interanimal similarities and dissimilarities.

Calculation of the uncertainties in the results in the new frame with error propagation formulas is not straightforward.

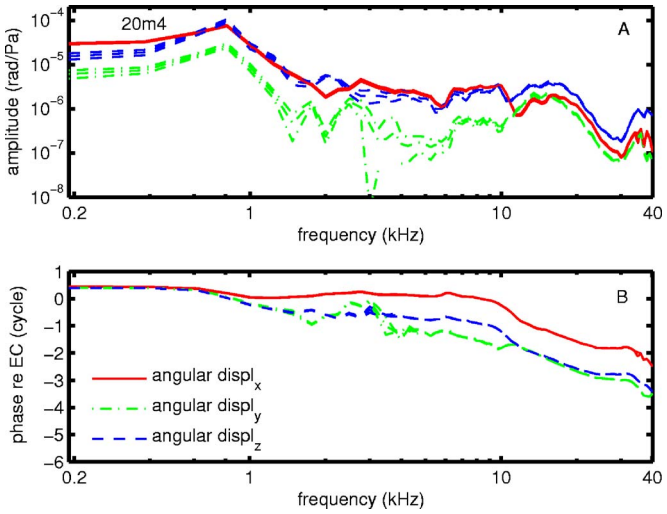

FIG. 9. (Color online) Frequency response for the rotation displacement components per EC sound pressure for animal 20m4 expressed in the intrinsic reference system as defined in Fig. 2. (A) Amplitudes and (B) phases. Uncertainties are shown by plotting component value + error and value − error curves.

The Monte Carlo technique can also be used to simplify this calculation. To produce random sets of rigid body motion components in the experimental reference frame we added to the fitted components Gaussian noise with a variance equal to $\frac{3}{4}$ of the standard errors (variances equal to the standard errors yielded some unrealistically large deviations when extreme values in the tails of the distribution were drawn). All these synthetic displacement components were converted in the intrinsic frame and the error on a given component was obtained as its standard deviation. The uncertainties are indicated with lines above and below the curves (parameter ± error) for each displacement component. As noted earlier, we see that peaks and valleys are genuine and not an artifact of the analysis.

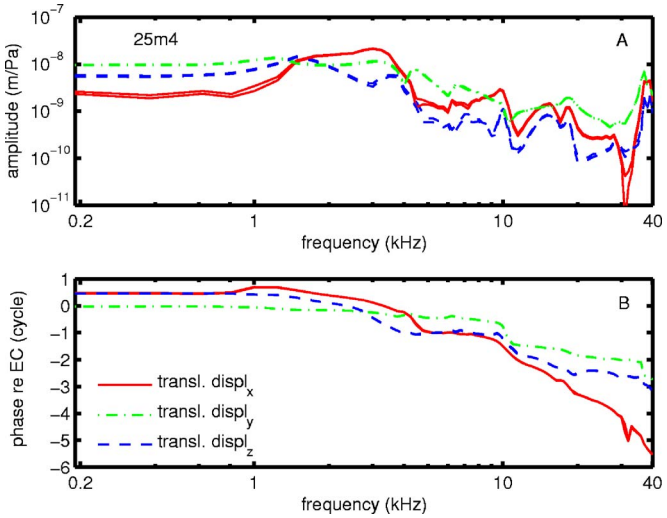

FIG. 10. (Color online) Frequency response for the translation displacement components per EC sound pressure for animal 25m4 expressed in the intrinsic reference system as defined in Fig. 2. (A) Amplitudes and (B) phases. Uncertainties are shown by plotting component + error and component − error curves. We see that peaks and valleys are genuine and that the piston component (dashed-dotted line) is most accurately determined (smaller error).

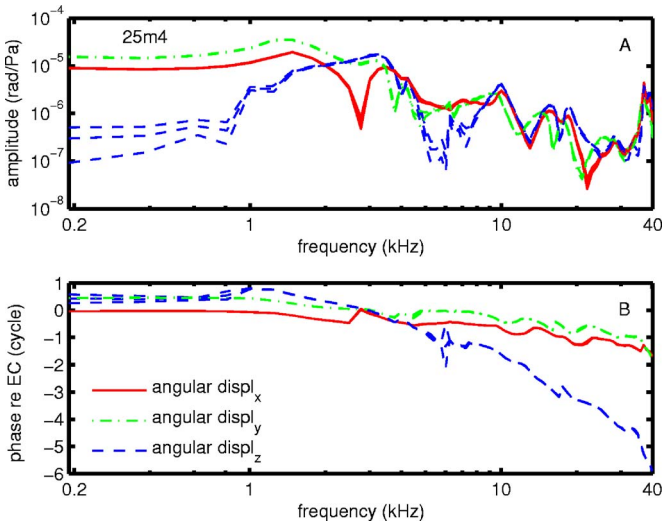

FIG. 11. (Color online) Frequency response for the rotation displacement components per EC sound pressure for animal 25m4 expressed in the intrinsic reference system as defined in Fig. 2. (A) Amplitudes and (B) phases. Uncertainties are shown by plotting component value + error and value − error curves.

a. Translation Plots of the frequency responses for the translation displacement amplitude per EC sound pressure for the three animals [Figs. 8(a), 10(a), and 12(a)] reveal similar features for corresponding components, with absolute levels of vibration differing about three to five times depending on the component up to 20 kHz and up to 10 times at the highest frequencies. Overall all translation components were of similar size, with the piston component (y axis) usually largest. The piston component was high and quite constant at low frequencies, peaked at about 1 to 2 kHz, decreased between 4 and 8 kHz, had a dip at about 5.8 kHz and a small peak at 8 kHz [Fig. 8(a)] or a dip at 6 kHz and a small peak at 7 kHz [Figs. 10(a) and 12(a)] and a small or more pronounced peak at 10 kHz in Figs. 8(a) and 10(a), respectively. Then it increased slowly to a broad maximum at about

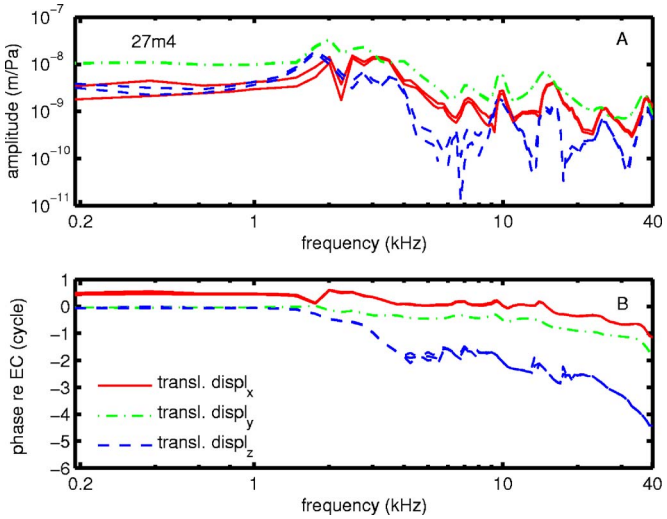

FIG. 12. (Color online) Frequency response for the translation displacement components per EC sound pressure for animal 27m4 expressed in the intrinsic reference system as defined in Fig. 2. (A) Amplitudes and (B) phases. Uncertainties are shown by plotting component value + error and value − error curves. We see that peaks and valleys are genuine and that the piston component (dashed-dotted line) is most accurately determined

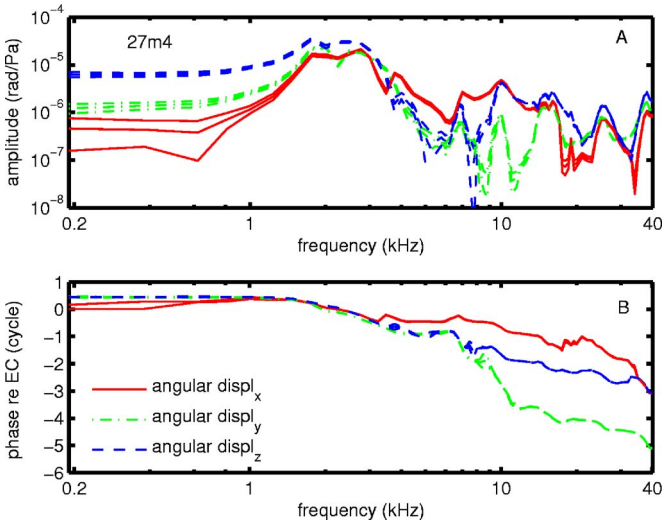

FIG. 13. (Color online) Frequency for the rotation displacement components per EC sound pressure for animal 27m4 expressed in the intrinsic reference system as defined in Fig. 2. (A) Amplitudes and (B) phases. Uncertainties are shown by plotting component value +/− error curves.

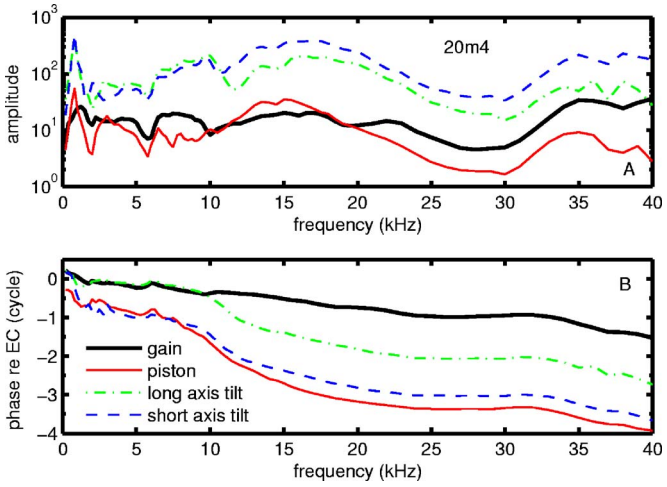

FIG. 14. (Color online) Amplitude (A) and phase (B) of the pressure gain (SV pressure relative to EC pressure, thick solid line) as a function of frequency for animal 20m4. The piston component velocity (thin solid line) and angular velocities about the long axis (dashed-dotted line) and short axis (dashed line) of the footplate are plotted as well to correlate pressure and velocity. To plot the amplitudes of the velocities on the graph in the scale of the gain, the piston velocity is expressed in units of 10^{-5} (m/s)/Pa, and the angular velocities in 10^{-3} (rad/s)/Pa.

15 kHz [Figs. 8(a) and 12(a)] or 18 kHz [Fig. 10(a)] followed by a decrease, fast in Fig. 8(a), slow in Figs. 10(a) and 12(a), to a minimum at 30 kHz. For higher frequencies it rose again to a maximum at 36 kHz of different height according to the animal. The in-plane translation along the long footplate axis (x) started out three times smaller that the piston component, but rose rapidly to become equal or even bigger than the piston component in a small frequency band around 2 kHz [Fig. 8(a)] or 3 kHz [Figs. 10(a) and 12(a)]. Then it decreased between 4 and 8 kHz but displayed peaks at the same frequencies as the y component. In Fig. 8(a) the x component peaked at 13 kHz at a value of half the y component and in Figs. 10(a) and 12(a) at 15 kHz to values slightly higher to equally high as the y component. The in-plane translation along the short footplate axis (z) had overall the lowest amplitude and the largest uncertainty. It had, as the other components, its highest amplitude at low frequencies and then dropped considerably. At 7 kHz [Fig. 8(a)], respectively, at 10 kHz [Figs. 10(a) and 12(a)] it showed a peak, also present in the corresponding y and z components, followed by a sharp dip. At around 15 kHz it rose again to a broad plateau. Two animals [Figs. 10(a) and 12(a)] showed a slight to more pronounced maximum at 28 and 25 kHz, respectively. After a dip at about 30 kHz the z components finally followed the same increasing trend to exhibit a maximum at around 37 kHz.

The phase of the piston component (y) for the three animals started out in-phase with the EC pressure at low frequencies. The phase remains zero up to the first peak in amplitude where a lag of about 0.25 cycle was observed [small step in Figs. 8(b) and Fig. 12(b), more gradual change in Fig. 10(b)], in agreement with a stiffness controlled system. In Fig. 8(b) the phase lag increased slowly and gradually below 10 kHz and much more rapidly above 10 kHz to reach about −3.5 cycle at 40 kHz. Phase lag accumulated with frequency in a very gradual way over the entire frequency range in Fig. 12(b). In Fig. 10(b) the phase took two steps-down of ~0.5 cycle in small frequency bands, accompanied by strong changes in amplitude [Fig. 10(a)] so that it ended up with larger total lag compared to Fig. 12(b).

Phases for the long footplate axis components (x) started with a lead of 0.5 cycle re pressure [Figs. 8(b), 10(b), and 12(b)]. The short footplate axis component (z) once led by 0.5 cycle [Fig. 10(b)] and twice started in-phase with pressure [Figs. 8(b) and 12(b)]. In Fig. 8(b) all phases follow roughly the same trend. Phases for y and z were quite similar in Fig. 10(b), in Fig. 12(b) this holds well for the x and y components.

b. Rotation. The angular displacements complementing the translation displacements of Figs. 8, 10, and 12 are given in Figs. 9, 11, and 13, respectively. The amplitudes (in rad/Pa) are shown in the upper panels (A) and the phases relative to EC in cycles in the lower panels (B). In Figs. 9(a), 11(a), and 13(a) the three curves are intertwined In Fig. 13(a) the angular displacement components differ more from one another than in Figs. 9(a) and 11(a). Generally the rotation amplitudes were at their highest around 1–3 kHz where also the respective translational amplitude peaked, exhibited peaks and valleys while decreasing to their lowest values at about 30 kHz in Fig. 9(a), 23 kHz in Fig. 11(a), and 35 kHz in Fig. 13(a) and then climbed again to a maximum at around 37 kHz. The peak seen in all translation amplitude components at 10 kHz was also present in all rotation amplitude components. The x-component phase started off twice at 0 [Figs. 11(b) and 13(b)] and once at 0.5 lead [Fig. 9(b)], all the y- and z- components at 0.5 cycle phase lead relative to EC pressure. The three animals showed no common trend in the way the rotation phase lag accumulated with frequency.

C. SV pressure versus piston velocity and footplate tilt

We calculated the stapes piston velocity per EC pressure for animals 20m4, 25m4, and 27m4 (data were shown previously as displacements in Figs. 8–13) and we compare these velocities (y component of the translation velocity, thin solid line) with the individual pressure gains (thick solid line) in Fig. 14 (20m4), Fig. 15 (25m4), and Fig. 16 (27m4).

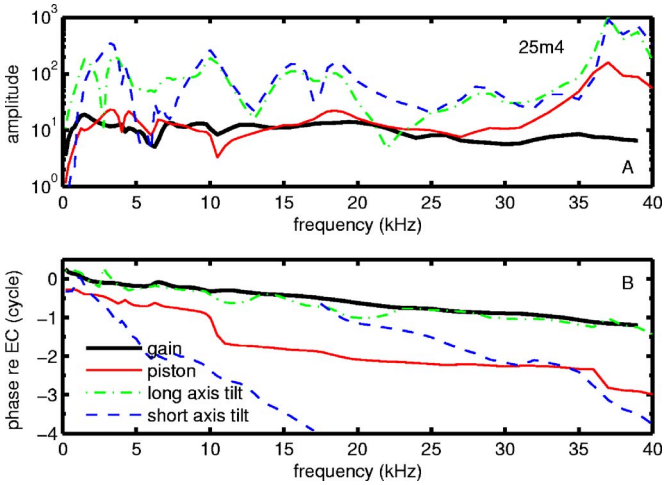

FIG. 15. (Color online) Amplitude (A) and phase (B) of the pressure gain (SV pressure relative to EC pressure, thick solid line) as a function of frequency for animal 25m4. The piston component velocity (thin solid line) and angular velocities about the long axis (dashed-dotted line) and short axis (dashed line) of the footplate are plotted as well to correlate pressure and velocity. To plot the amplitudes of the velocities on the graph in the scale of the gain, the piston velocity is expressed in units of 10^{-5} (m/s)/Pa, and the angular velocities in 10^{-3} (rad/s)/Pa. The discontinuity in the dashed phase curve is intentionally introduced by incrementing the phase angle with three cycles above ~17 kHz to enhance interpretation of the other curves on the graph (B).

To plot pressure and velocity on the same scale we multiplied the velocity by a scaling factor mentioned in the figure caption. To facilitate comparison over the entire frequency range we now use a linear frequency scale. It is clear that the pressure gain amplitudes [Figs. 14(a), 15(a), and 16(a)] were smooth functions of frequency. The piston component velocities relative to EC pressure amplitude were also relatively smooth, although less-so than pressure. In contrast, the footplate tilt showed considerable frequency structure. The gross trend of the curves for all three animals is fairly comparable. Differences between pressure and piston velocity were at the very lowest frequencies where the growth of the piston velocity with frequency was seen to be slower than the pressure gain growth with frequency. Some clear peaks in piston velocity amplitude, but of overall change in amplitude limited to ±66 dB, were not seen in the pressure (e.g., 25m4 at 3.5, 4.5, 18, and 37 kHz or 27m4 at 10 and 15 kHz). Some dips in the piston amplitude were accompanied by dips in the pressure (20m4: 5 and 30 kHz; 25m4: 6 and 10 kHz; 27m4: 6 kHz), but sometimes this was not true and a peak in velocity amplitude could even go along with a dip in pressure (27m4: 10 kHz). Disregarding these small wiggles the piston velocity was quite flat in a wide frequency band from 2.5 to 32.5 kHz for the three animals and the amplitude stayed high up to the highest frequencies measured. The pressure gain phase for all three animals [Figs. 14(b), 15(b), and 16(b)] winds approximately linearly down to a lag of about −1.5 cycle at 40 kHz (as already shown Fig. 4); the piston velocity phase in one case had a very similar excursion (27m4, Fig. 16) and in the others was more complicated.

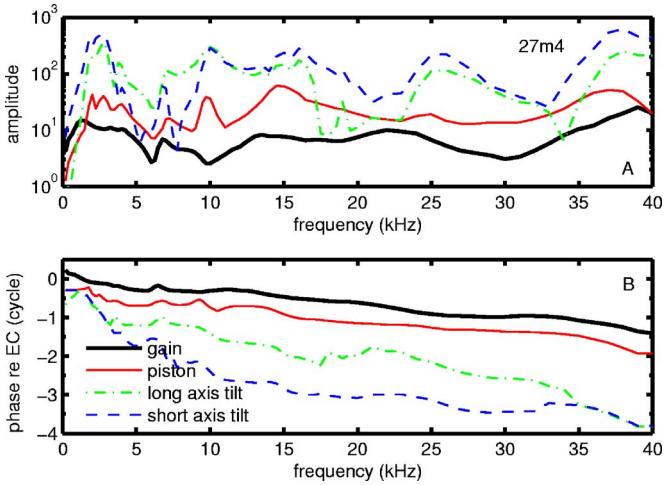

FIG. 16. (Color online) Amplitude (A) and phase (B) of the pressure gain (SV pressure relative to EC pressure, thick solid line) as a function of frequency for animal 27m4. The piston component velocity (thin solid line) and angular velocities about the long axis (dashed-dotted line) and short axis (dashed line) of the footplate are plotted as well to correlate pressure and velocity. To plot the amplitudes of the velocities on the graph in the scale of the gain, the piston velocity is expressed in units of 10^{-5} (m/s)/Pa, and the angular velocities in 10^{-3} (rad/s)/Pa.

Pressure in the inner ear is produced when the footplate compresses the fluid in the cochlea and therefore only displacements perpendicular to the footplate are expected to induce pressure. The motion components that give rise to such displacement are the piston component of the translation and the tilt of the footplate about its short and long axes. At first it seems reasonable to exclude the tilting from producing a pressure that can propagate further down the cochlea since the tilting motion around the origin at the footplate center does not result in a compression, merely a redistribution of the fluid at the stapes. Let us contrarily hypothesize that such rotations are also effective in sound transmission. Can we find evidence in our data to support this viewpoint? In the above, the piston velocity was less smooth than the SV pressure, and differed from the pressure in the details of the frequency response. We hypothesize therefore that stapes rotation fine tunes the transmission of sound by the ossicular chain in order to produce the smooth pressure response. To address this question we added to the plots of Figs. 14–16 the tilting components about the long (x axis, dashed dotted) and short (z axis, dashed line) footplate axes. The angular velocities were also scaled by a multiplier (see figure caption) so that again the same scale on the ordinate could be used. Angular components must be multiplied by the perpendicular distance to the concerned rotation axis in order to obtain the extra velocity in the piston direction that must be summed with the translation piston velocity; at the footplate center the extra velocity is zero and, e.g., for a point at the end of the long axis the extra velocity is half the length of the long axis (5×10^{-4} m) multiplied by the angular velocity (typically 10^{-1} rad/s) yielding 5×10^{-5} m/s, which is half the average translation piston velocity (piston velocity $\sim10^{-4}$ m/s). Angular displacement therefore contributes significantly to the velocity of individual points on the footplate. Footplate tilt is frequency dependent (causing vibration mode of the stapes to change with frequency) and if it affects the SV pressure it can be expected it will do so at frequencies with large tilt.

To explore the hypothesis that tilting modes contribute

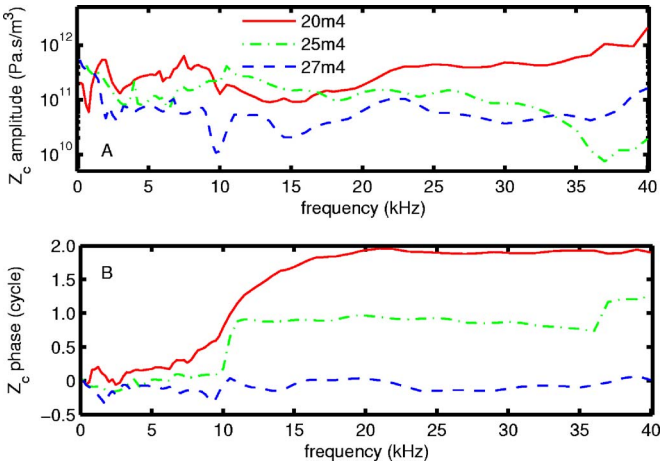

FIG. 17. (Color online) Cochlear input impedance Z_c [(A) amplitude; (B) phase] for all three animals (20m4, 25m4, and 27m4) as a function of frequency. The overall amplitude change over the very wide experimental frequency interval (200 Hz–40 kHz) remains small and this holds also for the phase if considered modulo 1 cycle.

to the pressure generation and play a role in smoothing the pressure gain versus frequency curve, we should look for frequency bands where the piston amplitude is small and where this is compensated by high angular amplitude. The effect does not have to be large as there were no frequencies where the piston amplitude went through a deep minimum. In fact, dips in piston amplitude were not systematically accompanied by peaks in tilt amplitude. A deep minimum in piston amplitude, not reflected in the pressure and accompanied by a peak in the tilt amplitude, would have supported the hypothesis, but it did not occur.

The data do not show any systematic relationship between footplate rotation and SV pressure, either in magnitude or phase. The fractional variations in rotation are in general bigger than the fractional variations in piston-translation and the rotation components are less related to pressure than the piston component is. This is particularly evident in Fig. 15. Therefore, the piston component and the SV pressure are relatively well related and the differences that do exist cannot be explained by rocking motion.

D. Input impedance of the cochlea

With the present data we can calculate the acoustic input impedance of the cochlea as the ratio of the pressure measured in the SV fluid behind the footplate to the volume velocity of the footplate. Pressure and velocity measurements were measured within an interval of 1–3 h in the same animals. The volume velocity was calculated as the piston velocity times the area of the footplate projected in the x-z plane (measured on one of our 3D stapes models as 0.62 mm^2). Results for the three animals used in the previous section are shown in Fig. 17. The three impedance amplitude curves [Fig. 17(a)] are all in the same range, and relatively flat over the most of the frequency range, except at frequencies above 35 kHz. Phase angle curves [Fig. 17(b)] differ from each other, but a closer look shows that the angle is mostly equal to values close to 0, 1, or 2 cycle. The 10 kHz step in the 25m4 curve might be due to the unwrapping of noisy data. The gradual and large phase excursion in the 20m4 curve is hard to explain, and needs to be repeated in truly simultaneous pressure and velocity measurements to warrant further interest.

IV. DISCUSSION

A. Scala vestibuli pressure and middle ear pressure gain

The present results on the SV pressure in gerbil are similar to results presented in previous papers of some of the present authors (Olson, 1998; Dong and Olson, 2006). Equipment and measuring procedure being the same this is to be expected and differences here are similar to the inter-animal differences found in those studies. Systematic sources of differences were discussed in Dong and Olson (2006).

In all three pressure gain curves shown (Fig. 4) we observed a pronounced dip in amplitude at about 6 kHz accompanied by a change in phase. We also found changes in vibration amplitude and phase occurring at the same frequencies (Figs. 8, 10, and 12). Similar changes in pressure and vibration were seen at comparable frequencies in gerbil experiments by Ravics *et al.* (1992), Teoh *et al.* (1997), and Rosowski *et al.* (1999). They showed that these were associated to resonances in a Hemholtz resonator formed by the bulla cavity and the hole made in the bulla wall, with the exact resonance frequency depending on the size of the hole.

B. Three-dimensional stapes motion

With our measuring technique we were able to determine the complete set of 3D rigid body motion components of the gerbil stapes, translational and rotational. In one experiment (20m4) almost the entire motion experiment was carried out while the animal was alive, the two other experiments were done in a just post mortem condition. We reported similar measurements for cat and human temporal bone previously (Decraemer and Khanna, 1997; Decraemer *et al.*, 2006).

The present measurements show larger deviations from piston motion than, e.g., our measurements on cat measured under similar experimental conditions enforcing velocity measurements with a large observation angle with the piston axis. To verify that this was not due to systematic error in our calculation we performed the following simulation experiment. We assumed that the piston performs a pure piston motion, with a frequency response as determined by one of our experiments (20m4). We calculated the amplitude and phase at the location of our experimental observation points for this motion in the experimental reference frame. We then applied Gaussian noise to these synthetic data (0.05 relative error on the amplitudes, 0.1 rad on the phase) and calculated the rigid body motion components for this data set in the intrinsic frame. We repeated this procedure 100 times and calculated the mean and standard deviations for the obtained motion components. The piston component obtained was perfectly in accordance with the piston component that we started out with. Translational motion components in the directions of the long and short axis were also produced but at all frequencies the amplitude of the component along the

short axis was about 20 times smaller than the experimental amplitude and about 30 times smaller for the short axis component. The simulation also produced rotation components but again with amplitudes that at all frequencies were at least 15 times smaller than the experimental values. Noise on the experimental observations is therefore not at the origin of the nonpiston components that came out of our experiments, these components must be really present.

We do not know any other study that measured the full 3D motion of the stapes or any other middle ear ossicle in gerbil or any other species. In one study on stapes motion in human temporal bones with normal air conduction stimulation, Hato *et al.* (2003) measured the stapes footplate vibration up to 10 kHz at five positions marked by reflective microspheres, one in the center and the four others at the ends of the long and short axis. The laser Doppler velocimeter beam was aimed through an opening made in the facial recess at an angle of 50°–60° from the direction perpendicular to the stapes footplate. A cosine correction was used to correct for this angle offset in the calculation of the stapes footplate motion. As all measurements were done with a fixed observation angle, only three motion components, i.e., the piston motion and the tilt about the long and short footplate axis could be determined. They reported that at frequencies below 1 kHz the piston-like motion of the stapes footplate dominated, whereas at higher frequencies it moved with increasingly complexity, with rotational motion along both the long and short axis. They also stated that above 3 kHz the stapes moved predominantly in a rotary fashion, reaching a peak at 6 kHz; above 6 kHz the rotary motion decreased slightly compared with the piston-like motion. Observations on the not purely piston-like character of stapes motion in human temporal bones were also made by Heiland *et al.* (1999) and Ball *et al.* (1997) based on relatively qualitative observations of 3D motion in human temporal bones.

In gerbil we found that the piston motion does not dominate so explicitly the vibration mode at low frequencies but nevertheless we see a clear reduction in angular displacement amplitude below 2 kHz [animal 25m4, Fig. 11(a) and 27m4, Fig. 13(a)] for all components by factors varying between 0.02 and 0.01. Differences in the mode of stapes vibration among gerbil, cat, and human may be due to the specific anatomy and differences in the condition of the ears during the measurements; gerbil: very tiny middle ear measured in live or very fresh cadaver condition, cat: a few hours post mortem as we waited until the response at a given point had stabilized, and human: largest and most sturdy of the three ears, untreated temporal bone measured a few days post mortem. One striking anatomical difference in these examples resides in the footplate asymmetry. In cat and gerbil the asymmetry is quite small compared to that in human, where the footplate—and this is no pun—really resembles the shape of a footprint with the posterior end much broader than the anterior end Decraemer *et al.* (2003).

To put a figure on the mode of vibration of the stapes footplate we have calculated the displacement of the superior end point of the short axis as a result of rotation about the long axis and the displacement of the posterior end of the long axis as a result of rotation about the short axis. We

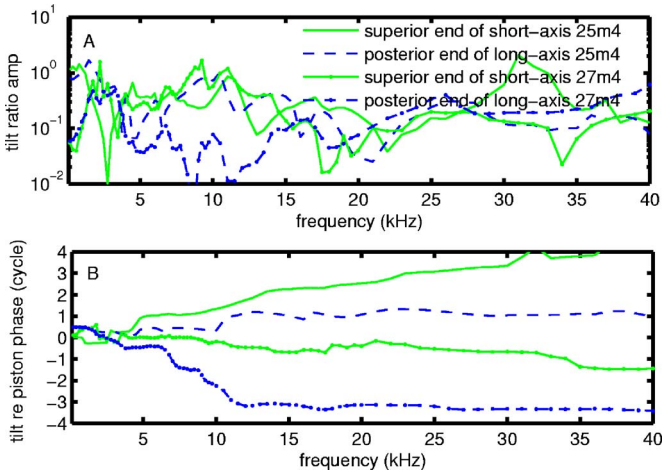

FIG. 18. (Color online) Comparison of displacement due to rotation about the long and short axis: the rotational displacement for the superior end of the short axis and the posterior end of the long axis are shown relative to the piston axis displacement. The amplitude (A) and phase (B) of this "tilt ratio" are shown as a function of frequency for animals 25m4 and 27m4.

plotted these displacements relative to the piston displacement for two animals (25m4 and 27m4) in Fig. 18. We see that for both animals the ratio of tilt to piston was the larger for the tilt about the short axis at almost all frequencies. Both "tilt ratio" amplitudes fluctuated with frequency, climbed to values greater than 1 at some frequencies, fell to values less than 1/100th at others, and were on average ~1/10. In certain frequency ranges tilts about short and long axis followed the same trend with frequency, but at other frequency ranges they were not correlated. The two animals showed strongly different tilt amplitudes. The plots of Fig. 18(b) show that the tilts about the long and short axes were not locked in phase, and that strong differences between the two animals were observed. We can conclude that in gerbil the piston component slightly dominates at frequencies below 2 kHz, but other components are also substantial and present throughout the entire frequency range.

Comments on the not purely piston-like character of stapes motion in gerbil were also made by Olson and Cooper (2000) based on a measurement of 3D motion of a single point on the posterior crus (by Cooper). In those studies, there appeared to be a transition from piston-like to more complex motion at ~6 kHz. Above this transition frequency, the motion was complex with substantial nonpiston motion, in accord with the present results.

C. Piston component measurement

Gerbil frequency responses of the stapes piston-velocity normalized by EC pressure were given by Rosowski *et al.* (1999) and Overstreet and Ruggero (2002). The velocity was measured using a unidirectional interferometer and an observation direction that made an angle with the piston axis because access for direct measurement of the stapes motion in line with the piston axis was not available. Rosowski *et al.* measured stapes motion up to 15 kHz, via 50 μm reflective plastic balls that were attached to the posterior crus via rubber cement and surface tension. The angle of incidence of the laser beam (Polytec laser vibrometer) was between 30° and

45° relative to the direction of the "piston-like" stapes translation, and a cosine correction was used to adjust the laser measurements to a value consistent with piston-like translation.

In the paper by Overstreet and Ruggero on high-frequency hearing sensitivity of the gerbil cochlea, stapes velocity was measured using a Dantec laser vibrometer (up to 40 kHz) focused on a reflective glass bead (diameter 20–30 μm) placed on the head of the stapes near the incudostapedial joint. They applied no correction to the measured velocity signal, arguing that the angle between the laser beam and the stapes vibration was always 30° or less.

The results of the two studies were very different. Rosowski *et al.* (1999) found stapes velocity features typical for a second-order spring-mass system, with a 6 dB/octave increase at low frequencies and a 6 dB/octave roll-off above 1.2 kHz. The phase varied from $+\pi/2$ to $-\pi/2$ between 50 Hz and 3 kHz, in accord with the spring-mass transition apparent in the amplitude.

Overstreet and Ruggero (2002, Fig. 2) show eight individual stapes velocity measurements as a function of frequency (500 Hz to 40 kHz) and their average. Each individual curve displays strong sudden fluctuations and between animals there are differences in level of up to 20 dB. The curves do not show a roll-off at higher frequencies, and the lack of high-frequency roll-off is emphasized in their results.

Our results agree and disagree with aspects of both studies. For animal 20m4 (Fig. 12) we saw a peak in piston velocity amplitude at about 1 kHz, with a phase transition in this frequency region of −0.5 cycle in agreement with Rosowski's study. While animals 25m4 (Fig. 15) and 27m4 (Fig. 16) showed a less pronounced local maximum near 1 kHz, the maximum in velocity amplitude occurred at about 2.5 kHz. The continued amplitude roll-off of Rosowski's curve is not seen in our measurements; we found a quite flat amplitude response all the way to the highest frequencies in accord with Overstreet. However, the dip in the frequency region <10 kHz could have been misinterpreted as the beginning of a roll-off if we had not extended our range of frequencies. The difference in frequency ranges explored in the different studies is likely the key to their different conclusions. In addition, calibration in the EC becomes somewhat ambiguous at high frequencies (above ~30 kHz in gerbil) and variations in calibration techniques can lead to systematic differences in results (Dong and Olson, 2006; Ravicz and Rosowski, 2004). Our average vibration levels were around 1×10^{-4} m/s Pa, which is in accord with the level of Rosowski (3×10^{-4} m/s Pa at the peak) and of Overstreet (average level ~3×10^{-4} m/s Pa).

Lets us point out further that the estimation of the stapes piston-velocity using an interferometer observation direction that makes a significant angle with the piston axis is prone to errors even when a cosine correction is applied (Decraemer *et al.*, 2006). This will further account for differences between our results based on a true 3D measurement and results from single axis observations (see also Sec. IV D).

D. Do nonpiston components influence scala vestibuli pressure?

1. Correlation of pressure and motion components

A deep minimum in piston-like amplitude that was not reflected in the pressure would have been a clear cut demonstration that pressure can also be produced by tilt components: We did not see this in any of the three animals (nor in a few preliminary experiments).

The overall trends of the SV pressure and piston amplitude curves (both relative to EC pressure) are the same (Figs. 14–16): Over almost the entire frequency range (0.2–40 kHz) the pressure gain was steady, fluctuations occurred over wide frequency intervals and were not very pronounced (<20 dB). Smooth fluctuations in piston amplitude, not repeated in the pressure amplitude, were seen, but these were more a strong ripple on a curve than a trend change in the curve. Pronounced peaks and valleys on the tilt amplitudes were not systematically reflected as valleys and peaks in the piston velocity, or were they apparent in the pressure. These arguments all sustain the conclusion that only the piston component was effective in producing pressure in the SV. With the present measurements it is impossible to rule out completely that tilt motion contributes to SV pressure production, but such a contribution would have to be small. The findings are in agreement with the idea that it is the net volume velocity of the footplate (piston velocity times footplate area; see also the next section) that produces the pressure in the SV directly behind the footplate. The tilt must cause the fluid to slosh back and forth in a small volume behind the footplate but the related pressure does not propagate further inward.

To our knowledge there are no previous studies where in an intact ear of any species the SV pressure was measured in combination with the complete 3D motion of the stapes. The closest to our measurements were the simultaneous SV pressure and stapes motion measurements in studies on cochlear input impedance (Z_c) of cat (Lynch *et al.*, 1982) and human temporal bone (Aibara *et al.*, 2001). Lynch *et al.* measured piston motion along the piston axis using a Mössbauer technique, Aibara *et al.* estimated the piston component from unidirectional interferometer measurements at the center of the footplate with a viewing angle of 35°–50° with the stapes axis (these angles are not given in the paper by Aibara, but were taken from papers of members of the same laboratory, referenced in context with the stapes motion measurement (Kurokawa and Goode, 1995; Heiland *et al.*, 1999)). Individual SV pressure and stapes piston motion curves are not shown in the Lynch *et al.* paper, therefore we will discuss it further in the section on impedance. Aibara *et al.* compare cochlear impedance magnitude with the stapes footplate rocking ratio found by Heiland *et al.* and concludes that a peak in the impedance curve at 6.5 kHz could be explained by a corresponding peak in the anterior/posterior rocking ratio curve, indicating that in this frequency region footplate motion is particularly complex and that a single point measurement at the center of the footplate is not adequate to determine the stapes piston motion. We would like to refine this statement: A measurement of center of footplate motion

under a large observation angle with the piston axis measures not only the cosine projection of the piston motion but it is also contaminated by the other translation components of stapes motion which, as we have shown, are present. However, truly rotation components about the footplate center will not contaminate the piston axis component estimate (Decraemer *et al.*, 2006) based on measurements at the center.

2. Footplate asymmetry and footplate volume velocity

The footplate (and its projection in a plane normal to the piston direction) is not flat but bowl shaped and it is asymmetric with respect to its long and short axes. Due to this asymmetry the tilt motion can produce a volume velocity that is not exactly zero (positive and negative part of the displaced volume not being equal). Earlier, we explored the hypothesis that tilt motion excites cochlear pressure experimentally; here we look at it theoretically, asking whether the tilt motion would in fact lead to net volume velocity into the cochlea at the stapes. In other words, what does a theoretical treatment have to say about the hypothesis that summing of the volume displacement due to piston and tilt acts as an integrating mechanism that fill in gaps of the piston volume displacement and smoothes the SV pressure?

The question could be answered by determining whether the volume velocity of the footplate is correctly calculated as the area of the footplate in the *x*-*z* plane times the piston velocity. We verified this by calculating directly the volume displaced by the footplate during its cyclic, 3D motion. The second calculation made no assumptions besides that the footplate is rigid. This was also one of the assumptions for the first calculation. As the footplate was not accessible during our experiments we have no real proof that it was indeed so. What we can say is that its bowl shape will make the footplate more rigid than if it were a flat plate. The footplate of the 3D stapes model can be described by a large number of small facets (small triangular, flat patch between three surface nodes). When the footplate is displaced a small volume (irregular pentahedron) is formed between the facet in its rest position and in its displaced position. We summed the volume for all the facets (954) of the footplate to obtain the displaced volume for the entire footplate. The calculation was repeated for 20 equally spaced time instants during a cycle. The obtained displacement as function of time within the cycle could be well fitted with a sinusoidal function (amplitude, phase). The volume displacement was converted to volume velocity. The calculation was done for all frequencies. The volume velocity obtained by integration was at all frequencies between 1% and 2% smaller than the simple calculation, *x*-*z* footplate area multiplied by piston velocity. The difference in phase was at all frequencies between −0.2° and +0.3°. Therefore, the simple multiplication is adequate and the asymmetry of the footplate does not give rise to an appreciable contribution to the footplate volume velocity caused by the tilt. In other words, the hypothesized integrating smoothing mechanism does not apply. This reinforces the experimental result, showing a lack of correlation between stapes rocking motion and cochlear pressure.

E. Cochlear input impedance

1. Gerbil

The only cochlear input impedance estimate for the gerbil is given by Overstreet and Ruggero (2002); it was obtained using the averaged stapes velocity measurement ($n=8$, range: 1–40 kHz) of their own and SV pressure measurements taken from Olson (1998). For the magnitude their value ranged between 1 and 2×10^{11} Pa s/m^5 while the phase ranged between 1/8 and 3/8 cycle. These values for the magnitudes were in good agreement qua overall level, but the details of the curves were quite different. We have calculated the cochlear impedances on an animal per animal basis using pressure and velocity data collected in the same animal and found significant inter-animal differences; Overstreet and Ruggero (2002, Fig. 6) used an average velocity with large standard deviation (see the discussion on stapes motion) and pressure data reported from experiments in another laboratory (Olson, 1998) to calculate Z_c. Strong differences in the precise trend of their and our Z_c curves are to be expected. Phase angles of Z_c by Overstreet are limited within 0 and 0.5 cycle, while our values extend beyond 1 cycle. The averaging process tends to wipe out jumps due to phase unwrapping that could be present in our measurements. Phase values that fall outside −0.25 and +0.25 cycle are hard to believe as they suggest that the cochlea is producing net sound power. The fact that the pressure and motion measurements were not made simultaneously is one explanation for the observation. Alternatively, when notches and rapid phase variations occur in the velocity small errors in measurement could introduce full cycle phase excursions, for example in Fig. 15, following the conversion between reference frames.

2. Cat

The pioneering measurements on cochlear input impedance by Lynch *et al.* (1982, Fig. 15, frequency range: 10 Hz–6 kHz) were performed on cat, therefore we can only use them for an interspecies comparison. The middle ear was drastically altered by removing the tympanic membrane, malleus and incus and constructing a new middle cavity over the oval window and the stapes. This impedance curve was not as smooth as our curves, but as the accuracy on the stapes motion measurement was of the order of ±3 dB, and on the SV pressure of the ±5 dB, the fluctuations may have been caused by experimental error. The frequency range 0.01–6 kHz was also different from our present curves. We have no measurements in the low frequency range (20–200 Hz) where a pronounced increase in Z_c magnitude is seen by Lynch *et al.* (1982, Fig. 15). From 200 Hz on, phases by Lynch hover between −45° and +45°. If we regard our phases modulo 1 cycle the two data sets are in quite good agreement in the overlapping experimental frequency region.

3. Human

Experiments on human cochlear impedance by Aibara *et al.* (2001, Fig. 4, frequency range: 500 Hz to 10 kHz) show large fluctuations on individual curves and large interindividual variation in all of the presented measurements, EC

sound pressure to stapes footplate velocity, and EC sound pressure to SV sound pressure, resulting in a large variability in Z_c magnitude and phase. The average magnitude level reported for human is $\sim 2 \times 10^{10}$ Pa·s/m^3, which is about ten times lower than our present value for gerbil. Their average phase angle remains small (range 0 to −60° or 0 to 1/6 cycle), which again is in agreement with our results, considered modulo 1 cycle.

V. CONCLUSION

We have presented measurements of the 3D velocity components of the stapes and have correlated these measurements with the SV pressure to verify whether nonpiston components of the footplate produce pressure behind the footplate and thus can give rise to an effective input to the cochlea and can help in realizing the remarkably smooth and flat pressure gain from ear canal to scala vestibuli as a function of frequency. We found no evidence for this hypothesis: Dips in the piston velocity were not systematically filled by peaks in tilt and conversely peaks in tilt were not apparent in the SV pressure. Further, we found that SV pressure and piston velocity correlated well overall but differences in trends of the curves were also present.

Although we collected pressure and velocity from the same individual animals, the measurements had to be made with a time interval between pressure and velocity measurements of at best 1 or 2 h, and sound source and EC microphone had to be taken out and replaced between the two experiment parts. During each experiment we experienced that pressure (SV and EC) and velocity measurements sometimes varied with time during the experiments, so differences between stapes piston velocity and SV pressure could be due to the fact that they were not simultaneously collected and to slight differences in the stimulus pressure. We therefore designed a new experimental protocol to measure piston velocity along a single axis and SV pressure at the same time. This ensures that the sound stimulus in the EC is exactly the same for both measurements. These experiments have been performed and will be reported in a follow-up paper.

ACKNOWLEDGMENTS

This work was supported by the NIH/NICDC (No. DC003130), the Emil Capita Fund, the Fund for Scientific Research (Flanders, Belgium), and Research Funds of the University of Antwerp. We thank S. Gea for the segmentation of the CT scan data.

APPENDIX A: ALIGNMENT OF THE CENTER OF ROTATION OF THE GONIOMETERS WITH THE FOCUSED LASER BEAM

Our setup is composed of an interferometer coupled to a confocal microscope (for a picture of the setup see Decraemer *et al.*, 1994a, Fig. 1; note that the axes in our actual experimental reference frame are inverted with respect to the situation shown in the insert: here the x axis is the same as in the insert (goes to the right), the y axis goes up, and the z axis toward the objective lens). The linear position of the object studied is controlled by a 3D linear positioning system. This positioning system can also be rotated around a vertical and a horizontal axis using a two goniometer system in a nested configuration. The outer horizontal goniometer rotates about a vertical axis (the y axis of our experimental reference frame), the inner goniometer about a horizontal axis. The goniometer base is adjusted to let the z axis of our experimental reference frame align with the interferometer observation direction (Fig. 19). In order to use the system optimally, the planes of focus of the microscope and the interferometer must be the same *and* the center of rotation of the goniometers must coincide precisely with the laser beam's focus. To this aim the goniometer base is mounted on crossed translational stages that can be repositioned in the x,z plane. The height (y axis) is adjusted by adding or removing thin metal sheets under the base of the goniometers. With the laser beam focused exactly at the center of rotation of the goniometers, the vibration of a given point can easily be studied from different angles, simply by rotating the goniometers. This appendix describes an efficient procedure for aligning the rotation center of the goniometers with the laser beam's focus.

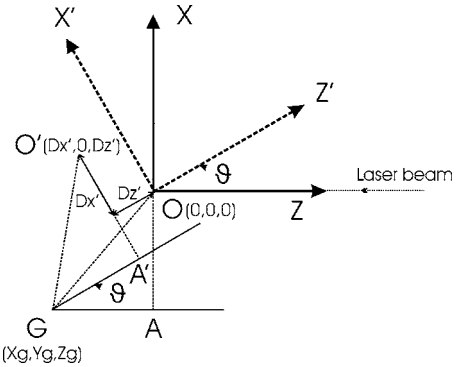

FIG. 19. O (0,0,0) is the origin of the sample's frame and corresponds to the point on the sample where the laser beam is focused. G is the position of the center of rotation of the goniometers. The distance between O and G is the "error" in alignment. After a rotation of θ about the y axis (points are rotated in the horizontal or $\hat{\mathbf{z}},\hat{\mathbf{x}}$ plane), point A becomes A', O becomes O' with $|\mathbf{AG}|=|\mathbf{A'G}|=|Z_g|$, $|\mathbf{OA}|=|\mathbf{O'A'}|=|X_g|$. With θ, X_g, and Z_g the correct base position can be calculated.

As an object we use a very thin wire (10 μm diameter) that we first mount in a vertical direction in a ring shaped holder (diameter ~10 mm). With both goniometers in their mid position (0°), the laser beam is focused on the wire. We let this point on the wire correspond to the origin O by resetting the linear coordinates to (0, 0, 0). The image of the wire and the position of the focused laser beam are traced on the screen of a video system with a marker.

Let us apply a rotation θ (θ corresponds to angle H in Appendix B) about the vertical axis (y). Looking down along the y axis in Fig. 19, we see that when G, the center of rotation of the goniometer, is not perfectly aligned with the focused laser beam, the point O rotates into a different point

O'. To bring this point back at the position of the laser focus we must move the object over a distance Dx' and Dz' that we can read off the linear scales.

The vector $\mathbf{OO'}$ can be expressed as a function of the coordinates of the center of rotation X_g, Z_g (vectors will be noted in bold; $\hat{\mathbf{x}}, \hat{\mathbf{z}}$ are unit vectors along x' and z' axes):

$$\mathbf{OO'} = Dx'\hat{\mathbf{x}}' + Dz'\hat{\mathbf{z}}',$$
$$\mathbf{OO'} = \mathbf{OG} + \mathbf{GA'} + \mathbf{A'O'} = X_g\hat{\mathbf{x}} + Z_g\hat{\mathbf{z}} - Z_g\hat{\mathbf{z}}' - X_g\hat{\mathbf{x}}'. \tag{A1}$$

After applying the coordinate transformation $\hat{\mathbf{z}} = \hat{\mathbf{z}}' \cos\theta - \hat{\mathbf{x}}' \sin\theta$ and $\hat{\mathbf{x}} = \hat{\mathbf{x}}' \cos\theta + \hat{\mathbf{z}}' \sin\theta$ we find

$$Dx' = X_g(\cos\theta - 1) - Z_g \sin\theta,$$
$$Dz' = X_g \sin\theta + Z_g(\cos\theta - 1) \tag{A2}$$

and

$$X_g = -\frac{Dx'}{2} + Dz' \frac{\sin\theta}{2(1-\cos\theta)},$$
$$Z_g = -Dx' \frac{\sin\theta}{2(1-\cos\theta)} - \frac{Dz'}{2}. \tag{A3}$$

Using these equations and the measured Dx' and Dz', distances X_g and Z_g can be calculated. To enhance accuracy the procedure is repeated for a number of increasing values of θ. The mean value of X_g and Z_g are calculated and used to adjust the position of the goniometer base in the x,z plane. The same procedure is performed with the wire mounted horizontally in order to determine Y_g and Z_g (Dy' and Dz' are measured for different V angles along the horizontal axis; we can reuse Eqs. (A2) and (A3) when we now let θ represent the angle $-V$). The height of the base of the goniometer is then adjusted following the calculated Y_g.

The centers of rotation of the vertical and horizontal goniometers were found to differ slightly in z direction (Z_g's obtained with V and H rotations differed by about 100 μm). The accuracy of the final alignment is therefore not perfect but for rotation less than 20° the displacement of the laser focus is less than 20 μm, and this was considered acceptable.

Remark that when X_g, Y_g, and Z_g are known for a not well aligned system we can calculate the observation point coordinates x,y,z in the reference system fixed to the interferometer, by subtracting Dx', Dy', and Dz' from, respectively, the coordinates x',y',z', recorded while the goniometers were turned.

APPENDIX B: CALCULATION OF THE 3D RIGID BODY VELOCITY COMPONENTS

To describe the stapes motion mathematically we use a stationary, inertial reference frame O_{xyz} attached to the interferometer. The origin of this fixed coordinate system is at the focus of the laser. In terms of the stapes, the origin is the point on the stapes that is in focus when the original vibration measurement was made (e.g., the zero position in Fig. 3). The stapes will be moved around and different points will be in focus when gathering the data to determine the motion, but the resulting description of 3D translational and rotational motion will refer to this original stapes position. The coordinate system is right-handed, with x axis horizontal to the right, y axis vertical up, and z axis along the (horizontal) observation direction toward the observer. General motion of a rigid body may be decomposed in a rotation about the origin O followed by a global translation of the body. The vector velocity of a point P_i of the rigid body (stapes) can be written as (vectors are denoted in bold)

$$\mathbf{v_i}(t) = \mathbf{v_t}(t) + \mathbf{\Omega}(t) \times \mathbf{r_i}, \tag{B1}$$

where $\mathbf{v_i}(t)$ is the velocity of P_i with components v_{ix}, v_{iy}, v_{iz} (this is the measured velocity); $\mathbf{v_t}(t)$ is the velocity of the global translational motion, with components v_{tx}, v_{ty}, v_{tz}; $\mathbf{\Omega}(t)$ is the angular velocity of the rigid body rotating about O, with components $\Omega_x, \Omega_y, \Omega_z$; $\mathbf{r_i}$ is the rest-position vector of point P_i with components x_i, y_i, z_i; and $\mathbf{\Omega}(t) \times \mathbf{r_i}$ is the velocity of the rotational motion component of P_i relative to O_{xyz}.

When the object is rotated using the goniometers, the vibration velocity vector $\mathbf{v_i}(t)$ rotates along with the object into a vector $\mathbf{v_i}(t)'$, where

$$\mathbf{v_i}(t)' = R(H_i, V_i) \cdot \mathbf{v_i}(t). \tag{B2}$$

$R(H,V)$ is the rotation matrix describing the rotation of the vector within the reference system of the interferometer. This rotation can be described as a first rotation about the y axis over an angle H, followed by a rotation over an angle V about the new position of the horizontal goniometer axis, resulting in

$$R(H,V) = \begin{vmatrix} R_{11} & R_{12} & R_{13} \\ R_{21} & R_{22} & R_{23} \\ R_{31} & R_{32} & R_{33} \end{vmatrix} = \begin{vmatrix} \cos(H) & 0 & \sin(H) \\ \sin(H)\sin(V) & \cos(V) & -\cos(H)\sin(V) \\ -\sin(H)\cos(V) & \sin(V) & \cos(H)\cos(V) \end{vmatrix} \tag{B3}$$

[the matrix shown here is a corrected version for the one in Decraemer *et al.* (1994a), where Eq. (B3) was not correctly printed].

For observation point i, the goniometers were at angles H_i and V_i and the corresponding rotation matrix $R(H_i, V_i)$ will be denoted R^i.

With the interferometer we observe only the component of vibration along the interferometer's viewing direction that coincides with our z axis,

$$v'_{iz} = |R^i_{31}\ R^i_{32}\ R^i_{33}| \cdot \begin{vmatrix} v_{tx} \\ v_{ty} \\ v_{tz} \end{vmatrix} + |R^i_{31}\ R^i_{32}\ R^i_{33}| \cdot \begin{vmatrix} z_i\Omega_y - y_i\Omega_z \\ x_i\Omega_z - z_i\Omega_x \\ y_i\Omega_x - x_i\Omega_y \end{vmatrix}. \tag{B4}$$

For all observation points ($i = 1, n$) we can write the following matrix equation:

$$\begin{vmatrix} v'_{1z} \\ v'_{2z} \\ \cdots \\ v'_{iz} \\ \cdots \\ v'_{nz} \end{vmatrix} = \begin{vmatrix} R^1_{31} & R^1_{32} & R^1_{33} & (y_1R^1_{33} - z_1R^1_{32}) & (z_1R^1_{31} - x_1R^1_{33}) & (x_1R^1_{32} - y_1R^1_{31}) \\ R^2_{31} & R^2_{32} & R^2_{33} & (y_2R^2_{33} - z_2R^2_{32}) & (z_2R^2_{31} - x_2R^2_{33}) & (x_2R^2_{32} - y_2R^2_{31}) \\ \cdots & & & & & \\ R^i_{31} & R^i_{32} & R^i_{33} & (y_iR^i_{33} - z_iR^i_{32}) & (z_iR^i_{31} - x_iR^i_{33}) & (x_iR^i_{32} - y_iR^i_{31}) \\ \cdots & & & & & \\ R^n_{31} & R^n_{32} & R^n_{33} & (y_nR^n_{33} - z_nR^n_{32}) & (z_nR^n_{31} - x_nR^n_{33}) & (x_nR^n_{32} - y_nR^n_{31}) \end{vmatrix} \cdot \begin{vmatrix} v_{tx} \\ v_{ty} \\ v_{tz} \\ \Omega_x \\ \Omega_y \\ \Omega_z \end{vmatrix}. \tag{B5}$$

This is an equation with the measured velocities in the left-hand side matrix and the design matrix (function of the angles H_i, V_i and the coordinates x_i, y_i, z_i which we will denote by I) multiplied by the matrix with the six unknowns at the right-hand side.

In the experiments we use a harmonic sound stimulus and as a consequence all functions of time t, namely v'_{iz}, v_{tx}, v_{ty}, v_{tz}, Ω_x, Ω_y, and Ω_z, become also harmonic and we can write

$$\begin{aligned} &v'_{iz} = A'_i \sin(\omega t + \vartheta_i), \\ &v_{tx} = v^0_{tx} \sin(\omega t + \varphi_{tx}), \quad v_{ty} = v^0_{ty} \sin(\omega t + \varphi_{ty}), \\ &v_{tz} = v^0_{tz} \sin(\omega t + \varphi_{tz}), \\ &\Omega_x = \Omega^0_x \sin(\omega t + \xi_x), \quad \Omega_y = \Omega^0_y \sin(\omega t + \xi_y), \\ &\Omega_z = \Omega^0_z \sin(\omega t + \xi_z). \end{aligned} \tag{B6}$$

Substituting these expressions in Eq. (B5), expanding the sine functions with the sum formula and equating the sin ωt and cos ωt terms results in the following two sets of equations:

$$\begin{vmatrix} A'_{1z} \cos \vartheta_1 \\ A'_{2z} \cos \vartheta_2 \\ \cdots \\ A'_{iz} \cos \vartheta_i \\ \cdots \\ A'_{nz} \cos \vartheta_n \end{vmatrix} = I \cdot \begin{vmatrix} v^0_{tx} \cos \varphi_{tx} \\ v^0_{ty} \cos \varphi_{ty} \\ v^0_{tz} \cos \varphi_{tz} \\ \Omega^0_x \cos \xi_x \\ \Omega^0_y \cos \xi_y \\ \Omega^0_z \cos \xi_z \end{vmatrix} \tag{B7a}$$

and

$$\begin{vmatrix} A'_{1z} \sin \vartheta_1 \\ A'_{2z} \sin \vartheta_2 \\ \cdots \\ A'_{iz} \sin \vartheta_i \\ \cdots \\ A'_{nz} \sin \vartheta_n \end{vmatrix} = I \cdot \begin{vmatrix} v^0_{tx} \sin \varphi_{tx} \\ v^0_{ty} \sin \varphi_{ty} \\ v^0_{tz} \sin \varphi_{tz} \\ \Omega^0_x \sin \xi_x \\ \Omega^0_y \sin \xi_y \\ \Omega^0_z \sin \xi_z \end{vmatrix}. \tag{B7b}$$

Using five observation directions with six to eight observation points each, these equations represent overdetermined systems of linear equation. They are solved separately for $v^0_{tx} \cos \varphi_{tx}$, $v^0_{ty} \cos \varphi_{ty}$, $v^0_{tz} \cos \varphi_{tz}$, $\Omega^0_x \cos \xi_x$, $\Omega^0_y \cos \xi_y$, and $\Omega^0_z \cos \xi_z$ (these are the components of the "in-phase" translation and rotation vectors $\mathbf{v_{tc}}$ and $\mathbf{\Omega_c}$—subscript c) and their sine counterparts $v^0_{tx} \sin \varphi_{tx}$, $v^0_{ty} \sin \varphi_{ty}$, $v^0_{tz} \sin \varphi_{tz}$, $\Omega^0_x \sin \xi_x$, $\Omega^0_y \sin \xi_y$, and $\Omega^0_z \sin \xi_z$ ("$\pi/2$ out-of-phase" vectors $\mathbf{v_{ts}}$ and $\mathbf{\Omega_s}$—subscript s). They are finally used to determine the six amplitudes ($v^0_{tx}\ v^0_{ty}\ v^0_{tz}\ \Omega^0_x\ \Omega^0_y\ \Omega^0_z$) and six phases ($\varphi_{tx}\ \varphi_{ty}\ \varphi_{tz}\ \xi_x\ \xi_y\ \xi_z$) that characterize the translation and rotation velocities. This procedure is repeated for each experimental frequency.

Let us note also that we can write $\mathbf{v}$ as $\mathbf{ds}/dt$ and $\mathbf{d\Omega}$ as $\mathbf{d\Theta/dt}$ so that multiplying both sides of Eq. (B1) by dt we end up with an equation between infinitesimal linear and angular displacements

$$\mathbf{ds_i}(t) = \mathbf{ds_t}(t) + \mathbf{d\Theta}(t) \times \mathbf{r_i}. \tag{B1'}$$

The middle ear vibration amplitudes are so small (of the order of 10^{-8} m per Pa for translation and 10^{-5} rad per Pa for rotation) that Eq. (B1′) can be used to describe the experimental displacements when we let the differentials denote the very small but finite displacements. It follows that the equations derived here for the velocities also hold to determine the translational and rotational displacements, if so preferred.

APPENDIX C: TRANSFORMING THE MOTION COMPONENTS INTO THE INTRINSIC FRAME

To bring the stapes in an intrinsic reference frame it is first rotated and then a shift of origin is applied. When we describe the rotation by a matrix $R_{\text{exp\_to\_int}}$, the in-phase and out-of-phase translation and rotation vectors $\mathbf{v_{tc}}$, $\mathbf{\Omega_c}$, and $\mathbf{v_{ts}}$, $\mathbf{\Omega_s}$ transform as

$$\mathbf{v_{tc\_rot}} = R_{\text{exp\_to\_int}} \cdot \mathbf{v_{tc}}, \tag{C1a}$$

$$\mathbf{v_{ts\_rot}} = R_{\text{exp\_to\_int}} \cdot \mathbf{v_{ts}}, \tag{C1b}$$

$$\mathbf{\Omega_{c\_rot}} = R_{\text{exp\_to\_int}} \cdot \mathbf{\Omega_c}, \tag{C2a}$$

$$\mathbf{\Omega_{s\_rot}} = R_{\text{exp\_to\_int}} \cdot \mathbf{\Omega_s}. \tag{C2b}$$

When the origin is shifted from O to O' (O' is chosen at the footplate center), a point i has a new position vector $\mathbf{r'_i}$, with

$$\mathbf{r'_i} = \mathbf{r_i} - \mathbf{OO'}. \tag{C3}$$

Substituting Eq. (C3) in Eq. (B1)

$$\mathbf{v_i} = \mathbf{v_t} + \mathbf{\Omega} \times (\mathbf{r'_i} + \mathbf{OO'}) = (\mathbf{v_t} + \mathbf{\Omega} \times \mathbf{OO'}) + \mathbf{\Omega} \times \mathbf{r'_i} \tag{C4}$$

or

$$\mathbf{v_i} = \mathbf{v_t'} + \boldsymbol{\Omega} \times \mathbf{r_i'} \tag{C5}$$

with

$$\mathbf{v_t'} = \mathbf{v_t} + \boldsymbol{\Omega} \times \mathbf{OO'}. \tag{C6}$$

Equation (C5) shows that the shift does not affect the rotation velocity, hence

$$\Omega_{c\_\mathrm{int}} = \Omega_{c\_\mathrm{rot}} \tag{C7a}$$

and

$$\Omega_{s\_\mathrm{int}} = \Omega_{s\_\mathrm{rot}}, \tag{C7b}$$

while Eq. (C6) shows how the translation velocity is transformed. Applying Eq. (C6) to Eqs. (C1a) and (C1b) yields finally

$$\mathbf{v_{tc\_int}} = \mathbf{v_{tc\_rot}} + \boldsymbol{\Omega_{c\_int}} \times \mathbf{OO'} \tag{C8a}$$

and

$$\mathbf{v_{ts\_int}} = \mathbf{v_{ts\_rot}} + \boldsymbol{\Omega_{c\_int}} \times \mathbf{OO'}. \tag{C8b}$$

Equations (C7) and (C8) can then be used to calculate the amplitude and phase of the translation and rotation velocities in the intrinsic frame of the stapes.

Aibara, R., Welsh, J. T., Puria, S., and Goode, R. L. (**2001**). "Human middle-ear sound transfer function and cochlear input impedance," Hear. Res. **152**, 100–109.

Ball, G. R., Huber, A., and Goode, R. L. (**1997**). "Scanning laser Doppler vibrometry of the middle ear ossicles," Ear Nose Throat J. **76**, 213–222.

Besl, P. J., and McKay, N. D. (**1992**). "A method for registration of 3-D shapes," IEEE Trans. Pattern Anal. Mach. Intell. **14**, 239–256.

Decraemer, W. F., de La Rochefoucauld, O., Olson, E. S., Khanna, S. M., and Dirckx, J. J. J. (**2006**). "Estimation of stapes piston motion from uniaxial interferometer measurements along observation directions at an angle with the piston axis is prone to substantial errors," in *Vibration Measurements by Laser Techniques: Advances and Applications*, edited by E. P. Tomasini (SPIE, Bellingham, WA), Vol. **6345**, Paper No. 6345_12 (CD-ROM).

Decraemer, W. F., Dirckx, J. J. J., and Funnell, W. R. J. (**2003**) "Three-dimensional modelling of the middle-ear ossicular chain using a commercial high-resolution x-ray CT scanner," J. Assoc. Res. Otolaryngol. **4**, 250–263.

Decraemer, W. F., and Khanna, S. M. (**1996**). "Malleus vibrations in the cat ear are three dimensional," Proceedings of the Diversity in Auditory Mechanics, Berkeley, CA, pp. 115–121.

Decraemer, W. F., and Khanna, S. M. (**1997**). "Vibrations on the malleus measured through the ear canal," Proceedings of Middle Ear Mechanics in Research and Otosurgery, Dresden, 19–22 September **1996**, edited by K. B. Hüttenbrink, pp. 32–39.

Decraemer, W. F., and Khanna, S. M. (**1999**). *New Insights in the Functioning of the Middle-Ear. The Function and Mechanics of Normal, Diseased and Reconstructed Middle-Ears*, edited by J. J. Rosowski and S. Merchant (Kugler, The Hague, The Netherlands), pp. 23–38.

Decraemer, W. F., and Khanna, S. M. (**2000**). "Three-dimensional vibration of the ossicular chain in the cat," *Vibration Measurements by Laser Techniques: Advances and Applications*, edited by E. P. Tomasini (SPIE, Bellingham, WA), Vol. 4072, pp. 401–411.

Decraemer, W. F., and Khanna, S. M. (**2003**). "Measurement, visualization and quantitative analysis of complete three-dimensional kinematical data sets of human and cat middle ear," Proceedings of the Middle Ear Mechanics in Research and Otology, Matsuyama, Japan, pp. 3–10.

Decraemer, W. F., Khanna, S. M., and Funnell, W. R. J. (**1994a**). "A method for determining three-dimensional vibration in the ear," Hear. Res. **77**, 19–37.

Decraemer, W. F., Khanna, S. M., and Funnell, W. R. J. (**1994b**). "Bending of the manubrium in cat under normal sound stimulation," in *Optical and Imaging Techniques*, edited by H. J. Foth, A. Lewis, H. Podbielska, M. Robert-Nicoud, H. Schneckenburger, and A. Wilson, Proceedings of Progress in Biomedical Optics, Europto Series, 8–9 September **1994**, Lille, France (SPIE, Bellingham, WA), Vol. 2329, pp. 74–84.

Decraemer, W. F., Khanna, S. M., Funnell, and W. R. J. (**2000**). "Measurement and modelling of the three-dimensional vibrations of the stapes in cat," *Proceedings of the Symposium on Recent Developments in Auditory Mechanics*, edited by H. Wada, T. Takasaka, K. Ikeda, K. Ohyama, and T. Koike (World Scientific, Singapore), pp. 36–43.

Dong, W., and Olson, E. S. (**2006**). "Middle ear forward and reverse transmission in gerbil," J. Neurophysiol. **95**, 2951–2961.

Guinan, J. J., and Peake, W. T. (**1967**). "Middle-ear characteristics of anesthetized cats," J. Acoust. Soc. Am. **41**, 1237–1261.

Hato, N., Stenfelt, S., and Goode, R. L. (**2003**). "Three-dimensional stapes footplate motion in human temporal bones," Audiol. Neuro-Otol. **8**, 140–152.

Heiland, K. E., Goode, R. L., Masanori, A., and Huber, A. (**1999**). "A human temporal bone study of stapes footplate movement," Am. J. Otol. **20**, 81–86.

Johnstone, J. R., Alder, V. A., Johnstone, B. M., Robertson, D., and Yates, G. K. (**1979**). "Cochlear action potential threshold and single unit thresholds," J. Acoust. Soc. Am. **65**, 254–257.

Khanna, S. M., Koester, C. J., Willemin, J. F., Dandliker, R., and Roskothen, H. (**1996**). "A noninvasive optical system for the study of the function of the inner ear in living animals," edited by V. Tuchin, *Selected Papers on Coherence Domain Methods in Biomedical Optics* (SPIE, Bellingham, WA), Vol. 2732, pp. 64–81.

Khanna, S. M., and Stinson, M. R. (**1985**). "Specification of the acoustical input to the ear at high frequencies," J. Acoust. Soc. Am. **72**, 577–589.

Kurokawa, H., and Goode, R. (**1995**). "Sound pressure gain produced by the human middle ear," Otolaryngol.-Head Neck Surg. **113**, 349–355.

Lynch, T. J., Nedzelnitsky, V., and Peake, W. T. (**1982**). "Input impedance of the cochlea in cat," J. Acoust. Soc. Am. **72**, 108–130.

Olson, E. S. (**1998**). "Observing middle and inner ear mechanics with novel intracochlear pressure sensors," J. Acoust. Soc. Am. **103**, 3445–3463.

Olson, E. S. (**2001**). "Intracochlear pressure measurements related to cochlear tuning," J. Acoust. Soc. Am. **110**, 349–367.

Olson, E. S., and Cooper, N. (**2000**). "Stapes motion and scala vestibuli pressure," Abstracts of the 23rd Annual Midwinter Research Meeting, St-Petersburg Beach, FL, Abstract No. 399. Accessible at the ARO website.

Overstreet, E. H. III, and Ruggero, M. A. (**2002**). "Development of wide-band middle ear transmission in the Mongolian gerbil," J. Acoust. Soc. Am. **111**, 261–270.

Press, W. H., Flannery, B. P., Teukolsky, S. A., and Vetterling, W. T. (**1989**). *Numerical Recipes* (Cambridge University Press, New York).

Puria, S., Peake, W. T., and Rosowski, J. J. (**1997**). "Sound pressure measurements in the cochlear vestibule of human-cadaver ears," J. Acoust. Soc. Am. **101**, 1–17.

Ravicz, M. E., and Rosowski, J. J. (**2004**). "High-frequency sound transmission throughthe gerbil middle ear," Abstracts of the 27th Annual Midwinter Research Meeting, Abstract No. 817. Accessible at the ARO website.

Ravicz, M. E., Rosowski, J. J., and Voigt, H. F. (**1992**). "Sound-power collection by the auditory periphery of the Mongolian gerbil Meriones unguiculatus. I. Middle-ear input impedance," J. Acoust. Soc. Am. **92**, 157–177.

Rosowski, J. J., Ravicz, M. E., Teoh, S. W., and Flandermeyer, D. (**1999**). "Measurement of middle-ear function in the Mongolian gerbil, a specialized mammalian ear," Audiol. Neuro-Otol. **4**, 129–136.

Teoh, S. W., Flandermeyer, D. T., and Rosowski, J. J. (**1997**). "Effects of pars flaccida on sound conduction in ears of Mongolian gerbil: acoustic and anatomical measurements," Hear. Res. **106**, 39–65.

Willemin, J. F., Dandliker, R., and Khanna, S. M. (**1988**). "Heterodyne interferometer for submicroscopic vibration measurements in the inner ear," J. Acoust. Soc. Am. **83**, 787–795